Additively manufactured biodegradable Zn-Mn-based implants with an unprecedented balance of strength and ductility

Huang, Chengcong; Wang, Yizhu; Yang, Fan; Shi, Yixuan; Zhou, Jie; Zadpoor, Amir A.; Xu, Wei; Li, Yageng; Wang, Luning; More Authors

DOI
10.1016/j.actbio.2025.02.047

Publication date
2025

Document Version
Final published version

Published in
Acta Biomaterialia

Citation (APA)
Huang, C., Wang, Y., Yang, F., Shi, Y., Zhou, J., Zadpoor, A. A., Xu, W., Li, Y., Wang, L., & More Authors (2025). Additively manufactured biodegradable Zn-Mn-based implants with an unprecedented balance of strength and ductility. *Acta Biomaterialia*, *196*, 506-522. https://doi.org/10.1016/j.actbio.2025.02.047

Acta Biomaterialia 196 (2025) 506–522

Contents lists available at ScienceDirect

Acta Biomaterialia

journal homepage: www.elsevier.com/locate/actbio

Full length article

Additively manufactured biodegradable Zn-Mn-based implants with an unprecedented balance of strength and ductility

Chengcong Huang [a,b], Yizhu Wang [a], Fan Yang [c], Yixuan Shi [a,b], Shangyan Zhao [a,b], Xuan Li [a,b], Yuchen Lu [a,b], Yuzhi Wu [a,b], Jie Zhou [d], Amir A. Zadpoor [d], Wei Xu [e,*], Yageng Li [a,b,*], Luning Wang [a,b,*]

[a] Beijing Advanced Innovation Center for Materials Genome Engineering, School of Materials Science and Engineering, University of Science and Technology Beijing, 30 Xueyuan Road, Haidian District, Beijing 100083, China
[b] Institute of Materials Intelligent Technology, Liaoning Academy of Materials, Shenyang 110004, China
[c] Department of Orthopaedics, Peking University Third Hospital, No. 49 North Garden Road, Haidian District, Beijing 100191, China
[d] Department of Biomechanical Engineering, Delft University of Technology, Delft 2628 CD, the Netherlands
[e] National Engineering Research Center for Advanced Rolling and Intelligent Manufacturing, Institute of Engineering Technology, University of Science and Technology Beijing, 30 Xueyuan Road, Haidian District, Beijing 100083, China

ARTICLE INFO

Keywords:
Additive manufacturing
Laser powder bed fusion
Zinc alloy
Mechanical properties
Biodegradation behavior
Biocompatibility

ABSTRACT

Additively manufactured (AM) biodegradable zinc alloys hold huge potential as promising candidates for bone defect and fracture repair, thanks to their suitable biodegradation rates and acceptable biocompatibility. However, the mechanical properties of AM zinc alloys developed so far, ductility in particular, fall short of the requirements for bone substitution. Here, we present Zn-1Mn and Zn-1Mn-0.4Mg alloy implants with unique microstructures, fabricated using laser powder bed fusion (LPBF). Notably, the LPBF Zn-Mn-Mg alloy exhibited an extraordinary balance of strength and ductility, with an ultimate tensile strength of 289 MPa, yield strength of 213.5 MPa, and elongation over 20 %, outperforming all previously reported AM zinc alloys. The simultaneously enhanced strength and ductility of the ternary alloy were attributed to the strong grain-refining effect of the Mg_2Zn_{11} second phase and the synthetic strengthening caused by the dispersion of the $MnZn_{13}$ and Mg_2Zn_{11} second phases inside the grains and at the grain boundaries. In addition, both alloys had similar rates of *in vitro* biodegradation (~0.15 mm/year), properly aligned with the bone remodeling process, while also demonstrating favorable biocompatibility and upregulating multiple osteogenic markers. The Zn-Mn-Mg alloy showed even better osteogenic potential than the Zn-Mn alloy, owing to the addition of Mg. The combined attributes of the LPBF Zn-Mn-Mg ternary alloy indicated huge potential for its use as a bone repair material, especially for load-bearing bone fixation.

Statement of significance: The mechanical properties of previously developed additively manufactured biodegradable zinc alloys, especially ductility, have not met the requirements for bone repair. Using laser powder bed fusion (LPBF), we fabricated Zn-1Mn and Zn-1Mn-0.4Mg alloy implants with unique microstructures. The LPBF Zn-Mn-Mg alloy demonstrated an exceptional balance of strength and ductility, achieving a tensile strength of 289 MPa, yield strength of 213.5 MPa, and elongation over 20 %, surpassing all reported AM zinc alloys. This study is the first to produce a directly printed biodegradable alloy meeting the mechanical requirements for bone fixation devices without post-processing. Additionally, the alloy exhibited moderate a biodegradation rate and excellent biocompatibility, underscoring its potential for load-bearing bone repair applications.

* Corresponding authors: Wei Xu, National Engineering Research Center for Advanced Rolling and Intelligent Manufacturing, Institute of Engineering Technology, University of Science and Technology Beijing, 30 Xueyuan Road, Haidian District, Beijing 100083, China; YagengLi and Luning Wang, Beijing Advanced Innovation Center for Materials Genome Engineering, School of Materials Science and Engineering, University of Science and Technology Beijing, 30 Xueyuan Road, Haidian District, Beijing 100083, China.
E-mail addresses: weixu@ustb.edu.cn (W. Xu), yagengli@ustb.edu.cn (Y. Li), luning.wang@ustb.edu.cn (L. Wang).

https://doi.org/10.1016/j.actbio.2025.02.047
Received 25 November 2024; Received in revised form 19 February 2025; Accepted 21 February 2025
Available online 22 February 2025

1. Introduction

Zinc (Zn) alloys have garnered significant attention in recent years as promising biodegradable metallic biomaterials due to their appropriate biodegradation rates and acceptable biocompatibility [1–3]. Several biodegradable zinc alloys have been developed and processed using conventional manufacturing techniques such as rolling, extrusion, and drawing, followed by heat treatment and machining [4–6]. However, these manufacturing techniques cannot produce implants with complex, customized geometries.

Additive manufacturing (AM) has been intensively developed to tackle the dilemma between freeform design and cost-effective manufacturability, enabling the precise creation of personalized and functionalized implants [2,7]. AM was applied first to biodegradable pure Zn with fully densified and porous structures [8,9]. AM porous Zn showed compressive mechanical properties compatible with cancellous bone, thereby possessing the capability for bone repair [10,11]. For bone fixation, however, the tensile properties of even solid AM Zn fall short of the design requirements [12–14], let alone those of porous AM Zn. Bone plates made of biodegradable metals, for example, typically require a yield strength exceeding 230 MPa, ultimate tensile strength above 300 MPa, and an elongation greater than 15–18 % [15]. However, AM pure Zn exhibits a tensile strength between 93 and 138 MPa and elongation from 7.6 to 14.2 % [16–18]. These clear deviations from the design requirements need to be remedied through the development of more biodegradable Zn alloys.

Alloying is a commonly applied strategy to improve the mechanical properties of biodegradable Zn, particularly its strength. Yang et al. [5] investigated the effects of eight alloying elements (*i.e.*, Mg, Ca, Sr, Li, Mn, Fe, Cu, and Ag) on the mechanical properties of extruded zinc alloys and concluded that Li and Mg were the most effective elements for strengthening. However, simultaneously increasing strength and ductility remains challenging. For example, Wen et al. [12] prepared a Zn-0.7Li alloy by LPBF and achieved an ultimate tensile strength exceeding 400 MPa, while the elongation was only ≈3 %. Our previous research [19] on the LPBF Zn-3Mg alloy fabricated at three different scanning speeds confirmed that the addition Mg to Zn could greatly increase the ultimate tensile strength (UTS) but at the cost of elongation. Breaking the strength-ductility tradeoff appears to be particularly difficult for AM Zn alloys because traditional methods used to achieve a desired strength-ductility balance by modifying microstructure *via* forming, such as rolling or drawing, are not at one's disposal. Therefore, optimizing the alloy composition becomes a particularly important option to strike a balance between strength and ductility for AM Zn-based biomaterials.

The findings of previous studies [20–22] suggest that Mn is an effective alloying element for enhancing the ductility of Zn alloys, with microalloyed Zn-Mn alloys exhibiting elongation values greater than 80 % after being subjected to conventional plastic deformation and heat treatment [21,23]. The ductility enhancement was attributed to particle-stimulated nucleation (PSN [24]) to form dynamically recrystallized grains in the Zn-Mn alloys during rolling and during room temperature tensile testing [21]. During plastic deformation, $MnZn_{13}$ particles stimulate the surrounding grains to initiate recrystallization, resulting in ultrafine Zn grains. These ultrafine grains play a coordinating role in uniform plastic deformation. Grain refinement, a well-established method to enhance both strength and ductility [25], can also be achieved *via* rapid solidification inherent in many of AM processes, especially laser-based ones, as demonstrated in a variety of metallic materials [26,27].

Although Mn significantly enhances the ductility of Zn, its contribution to strengthening is limited. To increase the strengths of Zn-Mn alloys, Mg may be chosen as a promising alloying element due to the grain-refining effect by the Mg_2Zn_{11} phase. In the case of AM Zn-3Mg alloy, Mg_2Zn_{11} has been shown to increase the alloy's strength by pinning grain boundaries and dislocations [19]. Additionally, Mg is biologically beneficial for bone health, as Mg^{2+} ion can effectively promote new bone formation by releasing calcitonin gene-related peptide (CGRP) from the sensory nerve fiber endings, accelerating the adhesion of bone marrow mesenchymal stem cells (BMSCs), up-regulating the expression of bone morphogenetic protein 2 (BMP-2) and vascular endothelial growth factor (VEGF), and inhibiting the activity of the nuclear factor-kappa B (NF-κB) pathway [28–30].

In this study, we successfully utilized LPBF to fabricate a Zn-Mn-Mg ternary alloy with a unique, refined microstructure, achieving an extraordinary combination of strength and ductility. This work represents the first instance of directly printed biodegradable zinc alloys meeting the stringent mechanical property requirements for temporary bone fixation devices without the need for post-processing. By systematically evaluating their mechanical properties, biodegradation behavior, and biocompatibility, we demonstrate that these alloys not only exhibit superior mechanical performance but also align with the physiological demands of bone healing.

2. Material and methods

2.1. Zn-Mn and Zn-Mn-Mg powders

Pre-alloyed Zn-Mn (1 wt% Mn) and Zn-Mn-Mg (1 wt% Mn and 0.4 wt % Mg) powders were prepared by using the plasma rotating electrode process (PREP) that resulted in nearly spherical morphologies (Fig. 1a, b). Zn-Mn alloy powder particles had coarse grains, while the Zn-Mn-Mg alloy powder particles displayed a dendritic microstructure (insets in Fig. 1a, b). The median particle sizes D_{50} were 38.2 μm for the Zn-Mn alloy powder and 42.5 μm for the Zn-Mn-Mg alloy powder (Fig. 1c, d). Inductively coupled plasma optical emission spectroscopy (ICP-OES, Agilent 5110, USA) determined the actual Mn content of the Zn-Mn alloy powder to be 1.01 wt%. In contrast, the Zn-Mn-Mg alloy powder contained 0.97 wt% Mn and 0.38 wt% Mg (Table 1).

2.2. Specimen preparation

Cylindrical (Φ10 × 10 mm) and flat (60 mm × 10 mm × 10 mm) Zn-Mn and Zn-Mn-Mg alloy specimens were fabricated using an LPBF machine (SLM 125 HL, SLM Solution Group AG, Germany) in a closed build chamber with an argon shielding gas atmosphere and a residual oxygen level below 30 ppm. The key parameters of the LPBF process included laser power P, scanning speed V, hatch spacing H, and layer thickness D. After preliminary testing, these parameters were set as follows: $P = 60$ W, $V = 900$ mm/s, $H = 60$ μm, and $D = 30$ μm for the Zn-Mn alloy specimens, and $P = 70$ W, $V = 600$ mm/s, $H = 70$ μm, and $D = 30$ μm for the Zn-Mn-Mg alloy specimens. A zigzag scanning pattern with a rotation angle of 67° in subsequent layers was applied.

2.3. Microstructural characterization

The microstructures of polished specimens were examined through optical microscopy (OM, Olympus, Japan) and scanning electron microscopy (SEM, Zeiss Gemini 500, Germany) equipped with energy dispersive spectroscopy (EDS, Oxford instruments, UK). The relative densities of the specimens were estimated by measuring the area fraction of pores in different regions of three OM images using ImageJ (National Institutes of Health, USA). Metallographic structures were revealed by etching the specimens with a 5 % nitric acid-alcohol solution. SEM was also utilized to observe the fracture surfaces of the tensile specimens. The distribution of the elements on the specimens' cross-section was analyzed using an electronic probe micro-analyzer (EPMA, JXA-IHP 200F, JEOL, Japan). The phases present in the powders and in the LPBF specimens were analyzed using an X-ray diffractometer (XRD, SmartLab, Rigaku, Japan) with Cu Kα radiation at a scan rate of 4°/min over a 2θ angle range between 20 and 80°.

Electron back-scattered diffraction (EBSD) was carried out to

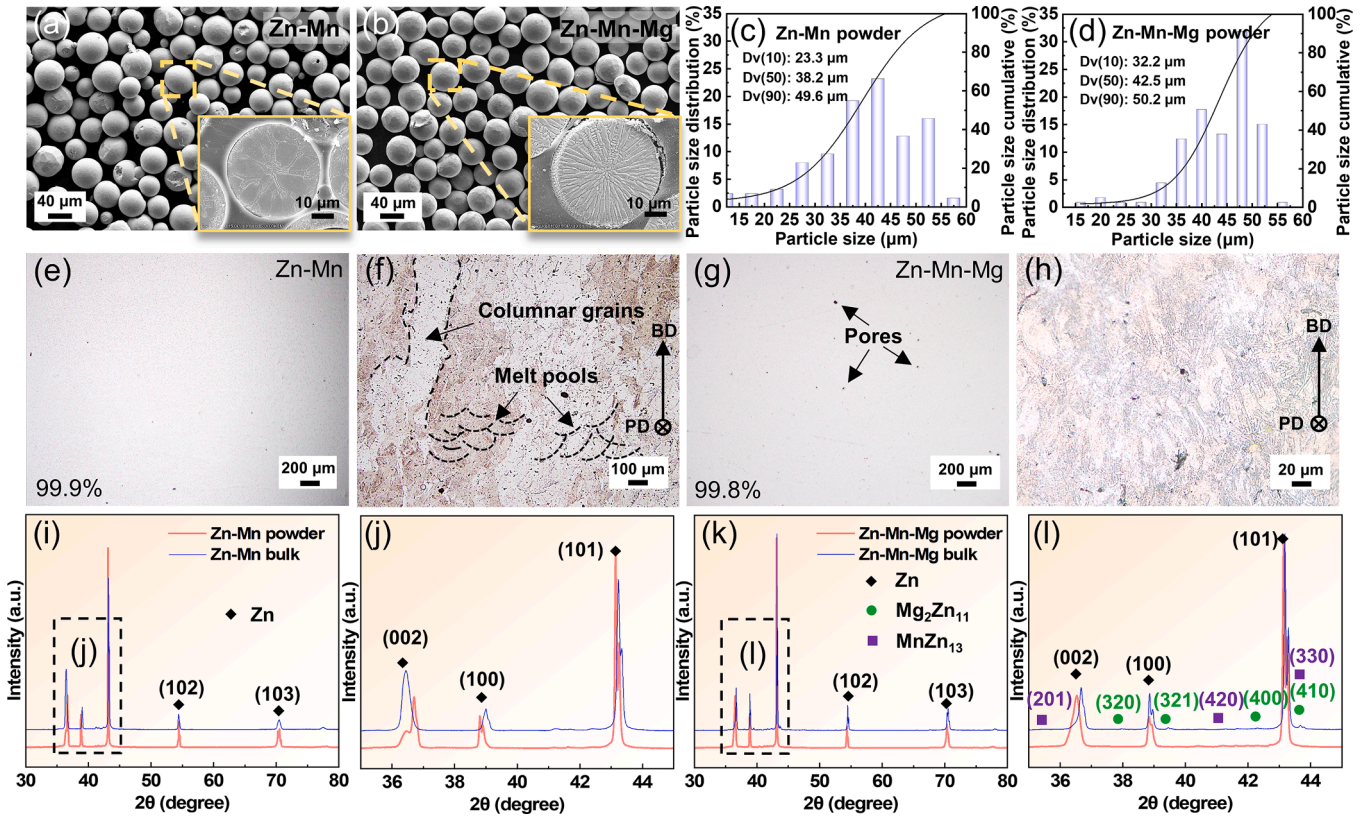

Fig. 1. Powder characterization and microstructure analysis of the LPBF specimens: (a, b) Zn-Mn alloy and Zn-Mn-Mg alloy powder morphology and internal structure, respectively, (c, d) Zn-Mn alloy powder and Zn-Mn-Mg alloy particle size distribution, respectively, (e, f) polished and etched surfaces of the LPBF Zn-Mn alloy specimen, respectively, (g, h) polished and etched surfaces of the LPBF Zn-Mn-Mg alloy specimen, respectively, (i, j) XRD spectra of the Zn-Mn alloy powder and LPBF specimen, and (k, l) XRD spectra of the Zn-Mn-Mg alloy powder and LPBF specimen.

Table 1
Chemical compositions of the Zn-Mn and Zn-Mn-Mg alloy powders.

wt %	Zn	Mn	Mg	O
Zn-Mn	98.9	1.01	0	<0.1
Zn-Mn-Mg	98.56	0.97	0.38	<0.1

investigate the grain structure by utilizing an Oxford Instruments AZtec analytical system attached to a SEM (SEM, Zeiss Gemini 500, Germany). Electrolytic polishing was used to prepare EBSD specimens. The polishing was performed in a solution containing 50 vol% H_3PO_4 and 50 vol % ethanol under a voltage of 5 V at room temperature for 15 s. The scanning area and step size were 912 μm × 692 μm and 1.2 μm for the Zn-Mn alloy specimens, while those were 72 μm × 56 μm and 0.12 μm for the Zn-Mn-Mg alloy specimens. Grain sizes were determined from the equivalent grain diameters, including the small grains at large grain boundaries and merged microcrystals, while grains with fewer than 100 pixels were excluded from the analysis. All the data were analyzed with the AZtecCrystal EBSD processing software (Oxford instruments, UK).

A transmission electron microscope (TEM, FEI Titan Cube 80–300, FEI Company, USA) working at 200 kV was used to investigate the microstructures further. Selected area electron diffraction (SAED) patterns and high-resolution TEM (HRTEM) were utilized to characterize the matrix and second phases. All the image data including those from Fast Fourier transform (FFT) in image processing were analyzed with the Gatan Microscopy Suite 3 (GMS 3) processing software (Gatan, USA). The specimens were sliced to a thickness of 1 mm, polished down to a thickness of 50–60 μm, punched into Φ3 mm discs, and finally thinned using a Gatan 695 ion thinner (Gatan, USA) at an initial angle of ± 4° and voltage of 5 kV.

2.4. Mechanical tests

Mechanical tests, including hardness, tension, compression, and three-point bending, were performed on Zn-Mn and Zn-Mn-Mg alloy specimens. The specimens were cleaned ultrasonically in ethanol prior to testing. The tension, compression, and three-point bending tests were conducted according to the GB/T 228-2021, GB/T 7314-2017, and GB/T 232-2010 standards, respectively. The tensile specimens were dog-bone-shaped with a thickness of 2 mm, the compressive specimens had a cylindrical shape (Φ10 × 15 mm), and the bending specimens had a rectangular shape (50 × 5 × 5 mm). The dimensions of these specimen were shown in Fig. S1. A universal testing machine (SHT4205, MTS, USA) was used for these tests at crosshead speeds of 0.001 s^{-1}, 0.001 s^{-1}, and 0.01 mm/min, respectively. For tension, an extensometer (632.18F-2x, MTS, USA) was used to measure deformation to obtain elastic moduli, and the non-sample displacement was not compensated for compression and three-point bending. The mechanical properties evaluated include tensile yield strength (TYS), compressive yield strength (CYS), ultimate tensile strength (UTS), ultimate compressive strength (UCS), and ultimate bending strength (UBS). The TYS and CYS were determined by offsetting the initial linear portion of the stress-strain curve by 0.2 % to find the yield strength intersection. The UTS represents the maximum strength on the stress-strain curve, while UCS indicates the stress at compressive fracture or at 60 % strain. Finally, UBS refers to the maximum stress applied to the specimen during bending, derived from the load *versus* cross-head displacement plots measured by the machine with high precision sensors and control systems. Vickers hardness ($HV_{0.2}$) (VTD512, China) was measured with a load of 200 gf, and ten measurements were made at the center of each specimen on the longitudinal section and parallel to the building direction (BD).

2.5. Electrochemical tests

The electrochemical performance of both LPBF alloys was evaluated using a typical three-electrode cell setup, with the Zn alloy as the working electrode, a platinum plate as the counter electrode, and a saturated calomel electrode as the reference electrode. The tests were conducted using an electrochemical workstation (ModuLab XM, AMETEK, USA) in a simulated body fluid (SBF [11]) at 37 °C. The electrochemical testing specimens had dimensions of Φ10 × 2 mm. Each specimen was positioned and secured within a mold having a circular opening with a diameter of Φ6 mm, ensuring that the surface area exposed to the simulated body fluid (SBF) was consistently maintained at 0.2826 cm^3. The open circuit potential (OCP) was monitored for 1800 s. Electrochemical impedance spectroscopy (EIS) test was performed at an amplitude of 5 mV and over a frequency range of 10^5 Hz to 10^{-2} Hz. Potential dynamic polarization (PDP) was determined at a scan rate of 1 mV/s. Nova 2.0 (Metrohm Autolab, Switzerland) and ZSimpWin 3.60 (Michigan, USA) were used for electrochemical data analysis. Corrosion potential (E_{corr}), corrosion current density (I_{corr}), and corrosion rate (CR_i) were calculated by line fitting and Tafel extrapolation (Table 2). The impedance data were analyzed via fitting to equivalent electrical circuits (Table 3). R_s, CPE_f and R_f are the solution resistance, capacitance and resistance of the biodegradation products, respectively. CPE_{dl} and R_{ct} are the double layer capacitance and charge transfer resistance, respectively, which are utilized to characterize the electrochemical interface of the electrolyte solution and the Zn substrate. χ^2 indicates the fitting quality.

2.6. In vitro immersion tests

In vitro immersion tests of the specimen were performed in the SBF [11] at 37 °C (pH 7.4) for up to 28 days. The dimensions of the Zn-Mn-based alloy specimens were Φ10 × 2 mm. The volume to surface area ratio was 20 ml/cm^2. After immersion, the biodegradation products were characterized with SEM, EDS, Fourier transform infrared spectrometry (FTIR, Vertex 70, Bruker, Germany), and X-ray photoelectron spectroscopy (XPS, Kratos AXIS-Ultra DLD, Shimadzu, Japan). Weight loss of the Zn alloy specimen was determined using an electronic balance (± 0.1 mg) after removing the biodegradation products with a 100 g/L ammonium chloride solution. Biodegradation rate (CR_w, mm/year) was calculated by using Eq. (1), according to ASTM G31–72 [31], where W represents the weight loss (g), A (cm^2) is the area of the specimen exposed to SBF, T (h) is the immersion time, and D (g/cm^3) is the density of the specimen. Three replicate specimens were measured for each condition. Zn^{2+} ion concentrations in the SBF were measured with ICP-OES (Agilent 5110, USA) at different time points.

$$CR_w = \frac{K \times W}{A \times T \times D} \quad (1)$$

2.7. Cell viability tests

Mouse osteoblast precursor cells (MC3T3-E1, ATCC-CRL-2594) were cultured in the α-MEM (alpha minimal essential medium, α-MEM, Gibco, USA) complete medium with 10 % fetal bovine serum (FBS, Gibco, USA) and 1 % penicillin streptomycin solution (Solarbio, China) at 37 °C, 5 % CO_2, and 95 % humidity. Extracts were prepared by incubating the Zn alloy specimens in α-MEM at an immersion ratio of 1.25 cm^2/mL for 3 days. 10 %, 20 % and 50 % extract concentrations were used for subsequent cell culturing, and α-MEM complete medium was utilized as a negative control, and α-MEM supplemented with 10 % dimethyl sulfoxide (DMSO, Invitrogen, USA) was used as a positive control. Cellular activity was measured after 1 day and 3 days using a CCK-8 assay (CCK8, Dojindo Molecular Technology, Japan). Optical density (OD) values were recorded at 450 nm (Bio-Tek, USA). As for the Live Dead assay, MC3T3-E1 cells were co-cultured with the extracts, stained with a live/dead cell staining kit (Solarbio, China) under protection from light, and observed under a fluorescence microscope (Zeiss, Germany).

In the cytoskeleton analysis, cells were seeded into 96-well plates and cultured with the extracts from the Zn alloy specimens for 24 h. After incubation, the cells were gently washed with a phosphate-buffered saline (PBS, Gibco, USA) solution to remove any excess medium, then fixated using 4 % paraformaldehyde at room temperature for 10 min to preserve cell structure. Following fixation, the cells were washed again with PBS and permeabilized using a 0.1 % Triton X-100 surfactant, which allowed the stains to penetrate the cell membranes. For visualization, two specific stains were applied: phalloidin-fluorescein isothiocyanate (FITC) (Sigma, USA), which bonds to and highlights the cellular actin filaments, and 2-(4-Amidinophenyl)-6-indolecarbamidine dihydrochloride (DAPI), which specifically stains the nuclei. The labeled cells were then examined under a fluorescence microscope (Zeiss, Germany).

The MC3T3-E1 cells were co-cultured with the 10 % and 20 % diluted extracts for assessment the bone regeneration ability, with α-MEM complete medium as the control group. Alkaline phosphatase (ALP) staining was carried out after 14 days of culture, with the extracts being refreshed every 2 days. The medium was removed and the cells were gently washed three times with PBS (Gibco, USA) at day 14. Then, the cells were fixed with formaldehyde and again rinsed gently three times with PBS buffer. ALP staining was performed with a 5-bromo-4-chloro-3-indolyl phosphate (BCIP)/nitro blue tetrazolium (NBT) alkaline phosphatase color development kit (Beyotime Biotechnology, China). The stained cells were visualized and analyzed by a fluorescence microscope (Zeiss, Germany). Expression levels of osteogenesis-related genes associated with collagen type I α1 chain (COL1), osteocalcin (OCN), and runt-related transcription factor 2 (RUNX2) were measured at day 14 with the real-time polymerase chain reaction (RT-PCR) technique. Gene expression analysis was performed using an ABI 7300 RT-PCR system (Applied Biosystems, USA).

2..8. Statistical analysis

The mechanical tests, electrochemical experiments, and cell experiments, were performed in triplicates, and all the experimental results were shown as mean ± standard deviation. All the results were analyzed using a two-way ANOVA test with a *post-hoc* Tukey's multiple comparison test, and Shapiro-Wilk analysis through SPSS Statistics 27 (IBM, USA) showed that all data were distributed normally. A significance level of $\alpha = 0.05$ was used for the analysis (No marking when $p > 0.05$; * represents $p < 0.05$; ** represents $p < 0.01$).

3. Results

3.1. Microstructures

The relative densities of the LPBF bulk Zn-Mn and Zn-Mn-Mg alloy specimens exceeded 99.5 %, as evidenced by microscopic images showing the presence of only a few microscale pores (Fig. 1e and g). Melt pool boundaries and columnar grains on the longitudinal section along the BD direction were observed in the Zn-Mn alloy specimens (Fig. 1f). In contrast, the Zn-Mn-Mg alloy specimens exhibited a randomly distributed fine acicular grain structure (Fig. 1h). XRD analysis of the LPBF Zn-Mn alloy specimens revealed the presence of the Zn matrix only without any detectable second phases (Fig. 1i and j), being the same as

Table 2
Biodegradation rates obtained from the PDP tests and immersion tests at day 28.

Specimen	E_{corr} (V/SCE)	i_{corr} (μA/cm^2)	CR_i (mm/year)	CR_w (mm/year)
Pure Zn	-1.19 ± 0.01	14.55 ± 0.1	0.22 ± 0.02	—
Zn-Mn	-1.21 ± 0.02	24.12 ± 0.2	0.36 ± 0.01	0.15 ± 0.01
Zn-Mn-Mg	-1.20 ± 0.02	29.60 ± 0.1	0.44 ± 0.01	0.14 ± 0.01

Table 3
EIS fitting parameters of the pure Zn, Zn-Mn and Zn-Mn-Mg specimens.

Specimen	R_s ($\Omega \cdot cm^2$)	CPE_f ($10^{-6}\ \Omega^{-1} \cdot s^n \cdot cm^{-2}$)	n_1	R_f ($k\Omega \cdot cm^2$)	CPE_{dl} ($10^{-4}\ \Omega^{-1} \cdot s^n \cdot cm^{-2}$)	n_2	R_{ct} ($k\Omega \cdot cm^2$)	χ^2 (10^{-4})
Pure Zn	70.47 ± 1.34	6.32 ± 0.44	0.73 ± 0.07	4.78 ± 0.40	3.23 ± 0.80	0.44 ± 0.09	31.18 ± 4.2	9.44 ± 0.52
Zn-Mn	48.02 ± 2.25	12.32 ± 0.43	0.59 ± 0.07	3.24 ± 0.14	4.59 ± 0.52	0.45 ± 0.01	15.44 ± 1.1	5.41 ± 0.36
Zn-Mn-Mg	62.3 ± 1.13	4.37 ± 0.45	0.73 ± 0.06	3.27 ± 0.06	2.05 ± 0.31	0.29 ± 0.1	264.4 ± 2.82	5.49 ± 0.15

the corresponding powder. However, peaks corresponding to the Mg_2Zn_{11} and $MnZn_{13}$ phases were detected in the XRD results of the LPBF Zn-Mn-Mg alloy specimens over a 2θ range of 35–45° (Fig. 1l). These peaks were hardly visible in the diffraction pattern of the corresponding powder.

Melt pool boundaries were clearly visible in the SEM images of the Zn-Mn specimens (Fig. 2a and b). EPMA images showed homogeneous distributions of Zn and Mn, with no apparent differences between the melt pool and its boundaries (Fig. 2e and f). However, the melt pool boundaries were not discernible on the longitudinal section of the Zn-Mn-Mg alloy specimen, which mainly consisted of acicular grains (Fig. 2c and d), being consistent with optical observations (Fig. 1h). A number of black second-phase particles were intermittently distributed at and within the acicular grain boundaries (Fig. 2d). EPMA revealed that the particles at the grain boundaries corresponded to Mn- and Mg-rich phases (Fig. 2i and j). It also confirmed the presence of oxides (Fig. 2j and k).

Orientation map revealed the columnar grains of the Zn-Mn alloy specimens, with an average grain size of 35 μm (Fig. 2l), while the Zn-Mn-Mg alloy specimens exhibited mainly acicular grains together with a few equiaxed grains and a much smaller average grain size of 2.8 μm (Fig. 2m). Notably, the kernel average misorientation (KAM) map (Fig. 2o) showed that the Zn-Mn alloy specimen had relatively high dislocation densities and local strains near the columnar grain edges, whereas the dislocation density and local strains were fairly low in the Zn-Mn-Mg alloy specimen (Fig. 2p).

TEM results (Fig. 3) show that two forms of the second phase were present in the Zn-Mn alloy specimens: a granular second phase and an

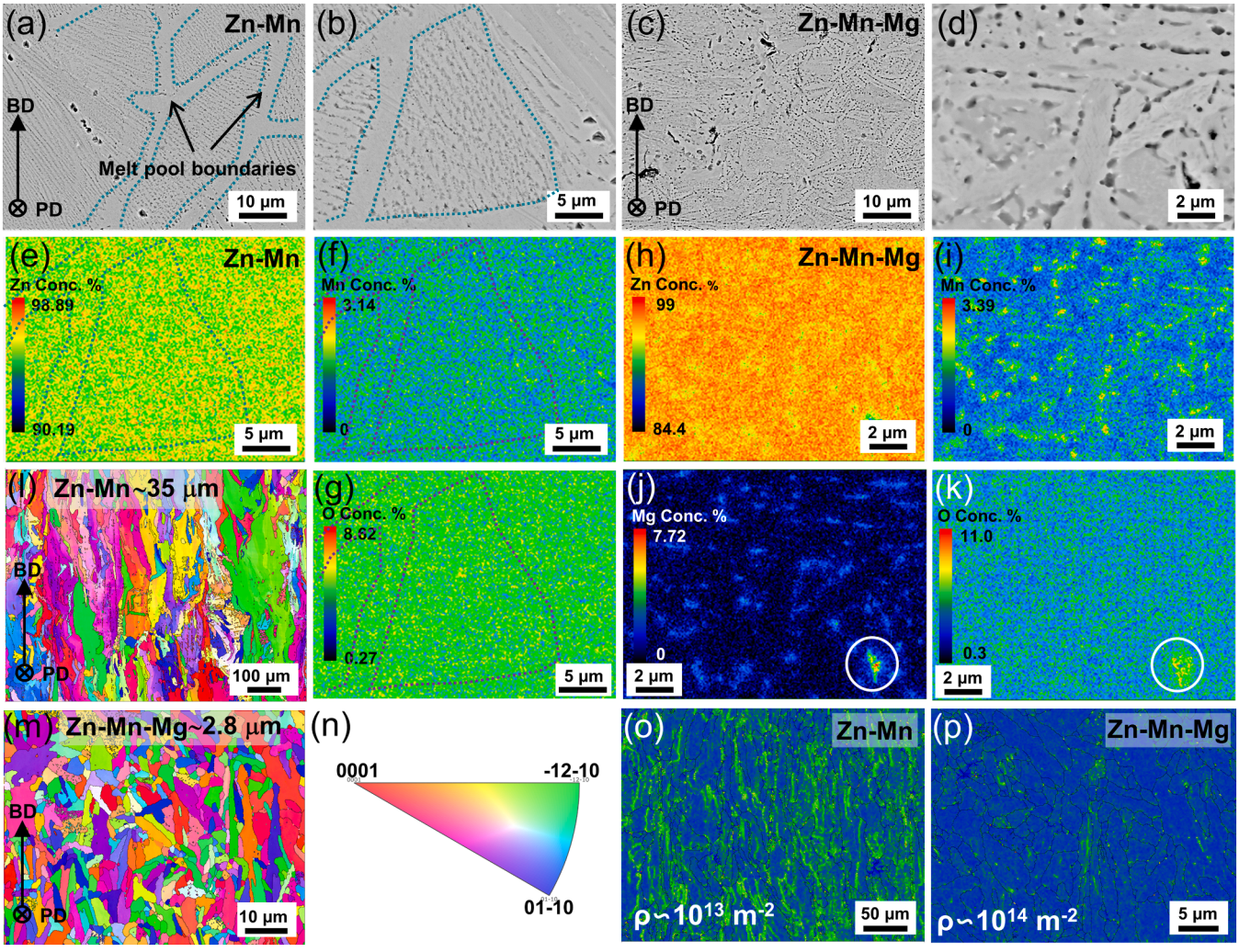

Fig. 2. Microstructure characterization of the LPBF specimens: (a-b and c-d) SEM images of the Zn-Mn and Zn-Mn-Mg alloy specimens, respectively, (e–g) corresponding EPMA images of the cross-section (b), (h–k) corresponding EPMA images of the cross-section (d), (l, m) orientation maps of the LPBF Zn-Mn alloy and Zn-Mn-Mg alloy specimens, respectively, (n) color coding corresponding to the grain orientations on the cross sections of (l) and (m), and (o, p) corresponding KAM maps of the localized areas of (l) and (m), respectively.

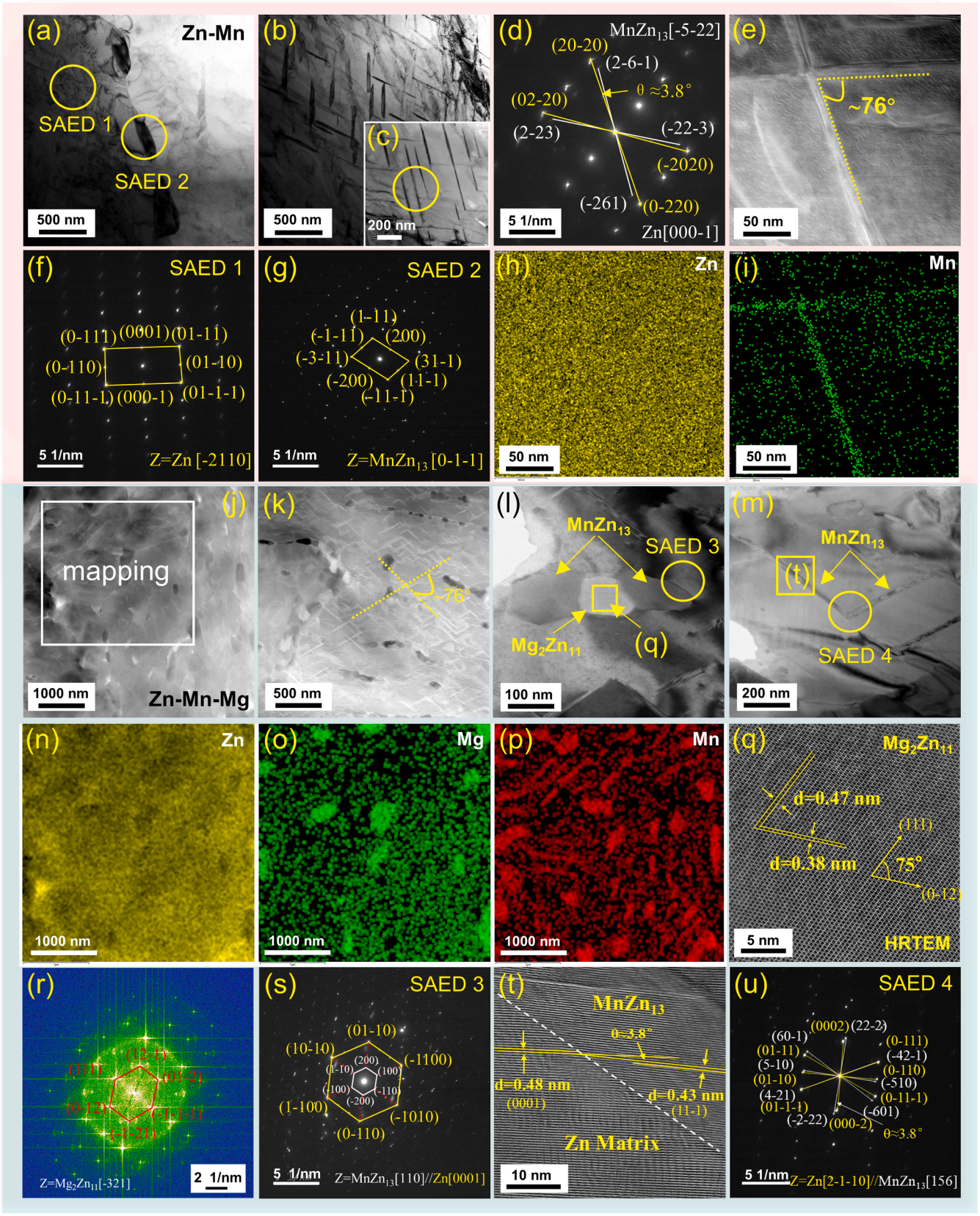

Fig. 3. TEM characterization of the LPBF specimens: (a–c, and e) TEM images of the Zn-Mn alloy specimen, (d and f-g) SAED of the Zn matrix and second phases in the images (a) and (c), (h, i) EDS mapping of the cross-section (d), (j–m) TEM images of the Zn-Mn-Mg alloy specimen, (n–p) EDS mapping of the cross-section (j), (q) HRTEM image of the second phase shown in (l), (r) FFT image corresponding to (q), (s, u) SAED patterns of the second phases in (l) and (m), respectively, and (t) HRTEM image of the second phase shown in (m).

acicular second phase (Fig. 3a and b). The former was mainly distributed discontinuously at the grain boundaries with sizes below 50 nm, which was identified as the $MnZn_{13}$ phase by SAED diffraction patterns (Fig. 3g). The acicular second phase was mainly distributed inside the grains with a width of about 25 nm. This second phase was identified as the $MnZn_{13}$ phase by SAED (Fig. 3d), and was staggered in a geometrical relationship at 76° (Fig. 3e). Notably, there was an orientation relationship between the Zn matrix and the acicular $MnZn_{13}$ phase with the zone axis of Zn $[000\bar{1}]$ // $MnZn_{13}$ $[5\bar{2}2]$ (Fig. 3d). Elemental mapping confirmed Mn enrichment inside the acicular second phase (Fig. 3i).

For the Zn-Mn-Mg alloy specimens, second phases were found both inside the grains and at the grain boundaries (Fig. 3j and k). Two types of second phases were distributed intermittently at the grain boundaries (Fig. 3l): one was identified by SAED as $MnZn_{13}$ (Fig. 3s), which had an orientation relationship between the Zn matrix and the zone axes of Zn [0001] // $MnZn_{13}$ [110]; the other one was identified as the Mg_2Zn_{11} phase by HRTEM and FFT (Fig. 3q and r). The acicular $MnZn_{13}$ phase inside the grains was similar to that in the Zn-Mn alloy specimens (Fig. 3b–d), staggered in a geometrical relationship at ~76° (Fig. 3k), but with an orientation relationship of Zn $[2\bar{1}\bar{1}0]$ // $MnZn_{13}$ [156] (Fig. 3u) and a lattice mismatch of ~3.8° (Fig. 3t and u). Analysis of elemental distribution verified that the particulate second phases at the grain boundaries contained Mn and Mg in addition to Zn, while the acicular second phase inside the grains contained Zn and Mn without Mg (Fig. 3n–p).

3.2. Mechanical properties

The tensile tests of the Zn-Mn-Mg alloy specimens showed significantly improved mechanical properties over the Zn-Mn alloy specimens (Fig. 4a). Both of the materials demonstrated a rapid increase in stress with increasing strain at the initial stage. The Zn-Mn alloy specimen exhibited a brittle behavior, as fracture occurred suddenly at a strain of around 0.44 %, and the 0.2 % offset line did not cross the stress-strain curve before the start of the softening phase (Fig. 4a), and, as a result, the yield point did not appear. In contrast, the Zn-Mn-Mg alloy

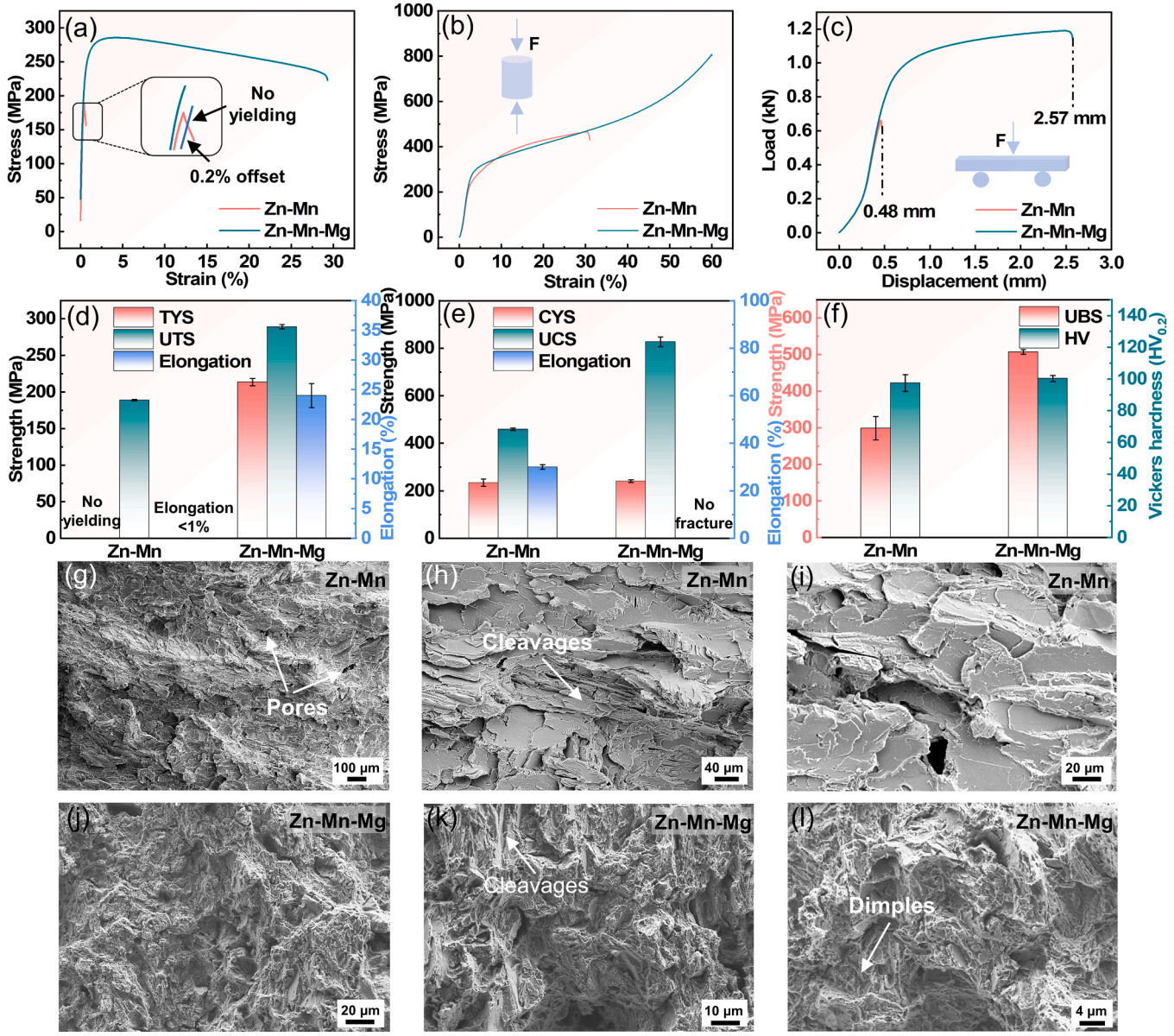

Fig. 4. Mechanical properties and fractography: (a) tensile stress-strain curves, (b) compressive stress-strain curves, (c) bending force-displacement curves, (d) tensile properties, (e) compressive properties, (f) bending and hardness properties, and (g–i and j–l) tensile fractography images of the LPBF Zn-Mn and Zn-Mn-Mg alloy specimens, respectively.

specimens had a much larger elongation value of 24 ± 2 % (Fig. 4a). The average UTS of the Zn-Mn alloy specimens was 189 ± 1 MPa, while the average UTS and TYS of the Zn-Mn-Mg alloy specimens were 289 ± 3 and 213.5 ± 5 MPa, respectively (Fig. 4d). According to the slope of the initial portion of the tensile stress-strain curves, the elastic moduli of the Zn-Mn and Zn-Mn-Mg alloy specimens were 61 ± 1 and 68 ± 4 GPa, respectively.

During the compression tests, both of the materials exhibited similar initial stress-strain behaviors, with stress continuously increasing with strain (Fig. 4b). The average CYS of the Zn-Mn-Mg alloy specimens (240.5 ± 6 MPa) was close to that of the Zn-Mn alloy specimens (234.5 ± 15 MPa) (Fig. 4e). However, the Zn-Mn specimens failed when the compressive strain reached approximately 30 %, with an average UCS of 459 ± 5 MPa. In contrast, the Zn-Mn-Mg alloy specimens did not fracture even when the strain reached 60 % (Fig. 4e).

During the three-point bending tests, the Zn-Mn alloy specimens fractured at a crosshead displacement of about 0.5 mm, while the Zn-Mn-Mg alloy specimens withstood the strain up to a machine displacement of 2 mm before failure (Fig. 4c). The average UBS values of the Zn-Mn and Zn-Mn-Mg alloy specimens were 298.6 ± 32 and 507 ± 6 MPa, respectively (Fig. 4f).

Although the Zn-Mn-Mg alloy specimens had much higher average UTS, UCS, and UBS values, as compared to those of the Zn-Mn alloy specimen, there was no statistically significant difference ($p = 0.14$) between the average HV values of Zn-Mn-Mg alloy specimen (100.3 ± 2) and Zn-Mn alloy specimen (97.4 ± 5.2) (Fig. 4f).

Tensile fractography revealed some pores on the fracture surface of the Zn-Mn alloy specimens (Fig. 4g) and numerous facets, typical of quasi-cleavage or cleavage fracture (Fig. 4h). In contrast, the Zn-Mn-Mg alloy specimens exhibited both cleavage fracture characteristics (Fig. 4j and k) and numerous minor dimples (Fig. 4l).

3.3. Electrochemical behavior

The potentiodynamic polarization (PDP) curves of the pure Zn, Zn-Mn and Zn-Mn-Mg alloy specimens showed similar trends, with the passivation behavior observed in the anodic area (Fig. 5a). According to the fitting results of the PDP curves, the Zn-Mn-Mg alloy specimen had higher values of I_{corr} and CR_i than the pure Zn and Zn-Mn alloy specimens (Table 2). The phase angles of the Zn-Mn-Mg alloy specimen were larger than those of the Zn-Mn alloy specimen at low and medium frequencies (Fig. 5b). The impedance modulus $|Z|$ of the Zn-Mn alloy specimen was smaller than that of the Zn-Mn-Mg alloy specimen at low frequencies, but their difference was minor at high frequencies (Fig. 5c).

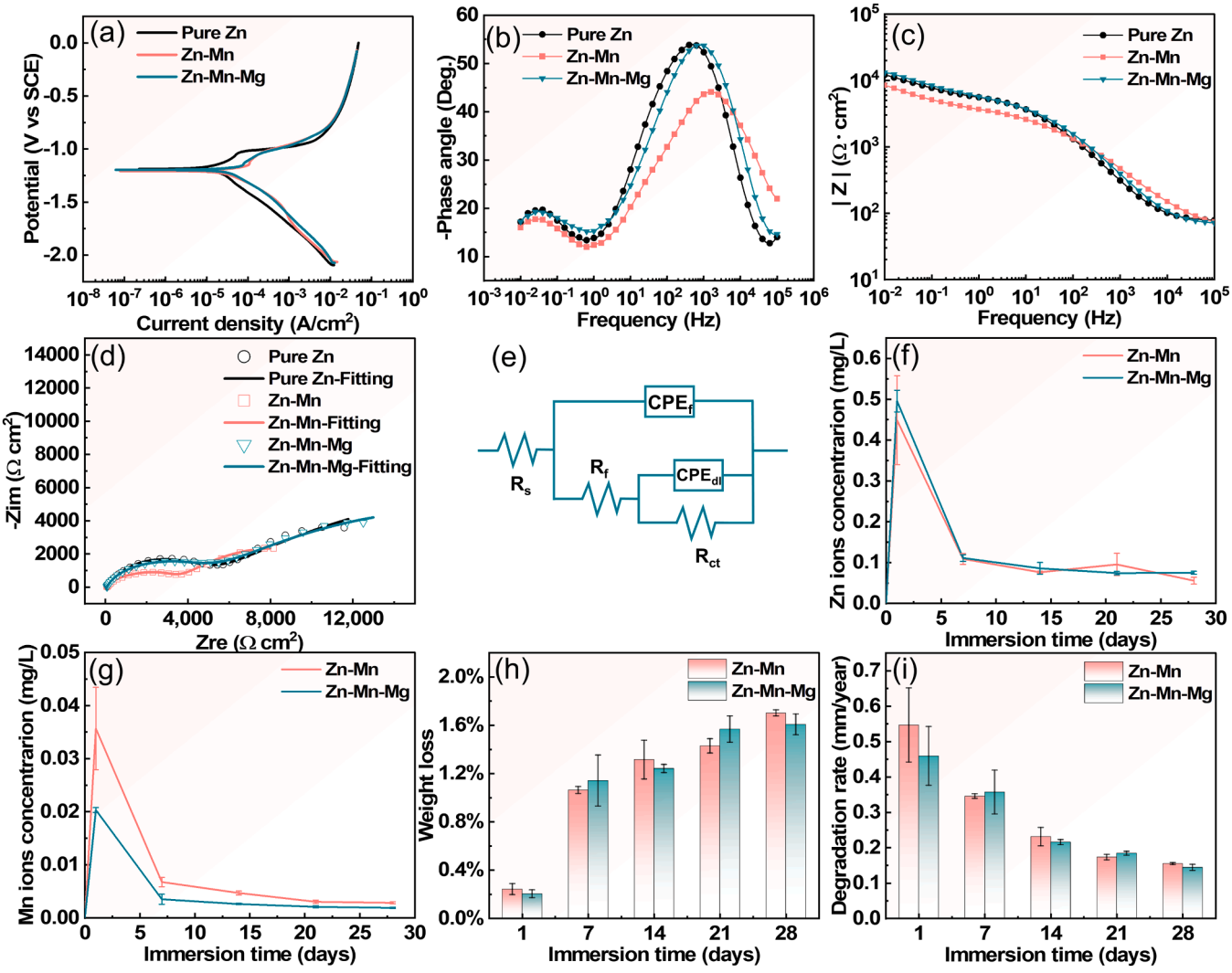

Fig. 5. Electrochemical behavior and *in vitro* biodegradation test results: (a) PDP curves, (b) Bode plots of phase angle against frequency, (c) Bode plots of impedance modulus |Z| against frequency, (d) Nyquist plots, (e) the equivalent circuit, (f) the variation of Zn^{2+} release from the LPBF specimens with changing immersion time, (g) the variation of Mn^{2+} release from the LPBF specimens with changing immersion time, (h) the weight losses of the LPBF specimens at various immersion time points, and (i) the biodegradation rates of the LPBF specimens at various immersion time points.

The Nyquist curves of both materials were composed of a semicircle and a straight line (Fig. 5d). The semicircle diameter of the pure Zn specimen was closed to that of the Zn-Mn-Mg alloy specimen, and both were significantly larger than that of the Zn-Mn alloy specimen. According to the fitted equivalent circuit (Fig. 5e and Table 3), the Zn-Mn-Mg alloy specimen showed larger R_{ct} value but smaller CPE_f and CPE_{dl} values than those of the pure Zn and Zn-Mn alloy specimens. χ^2 values of both materials were lower than 10^{-3}, indicating a close fit between the measured and expected values.

3.4. *In vitro* biodegradation behavior

For both materials, the rate of Zn ion release into the SBF decreased gradually with immersion time, with the maximum concentration (about 0.45 mg/L) reached at day 1 (Fig. 5f). The Mn ion release profile appeared to be similar to the Zn ion release profile, with the Zn-Mn alloy specimens exhibiting greater release rates than the Zn-Mn-Mg alloy specimens at all the time points (Fig. 5g). The weight loss of both types of specimens increased gradually with immersion time (Fig. 5h). After 28 days of immersion, the Zn-Mn and Zn-Mn-Mg alloy specimens had weight losses of 1.7 % and 1.6 %, respectively. The biodegradation rates of the Zn-Mn and Zn-Mn-Mg alloy specimens were calculated at various

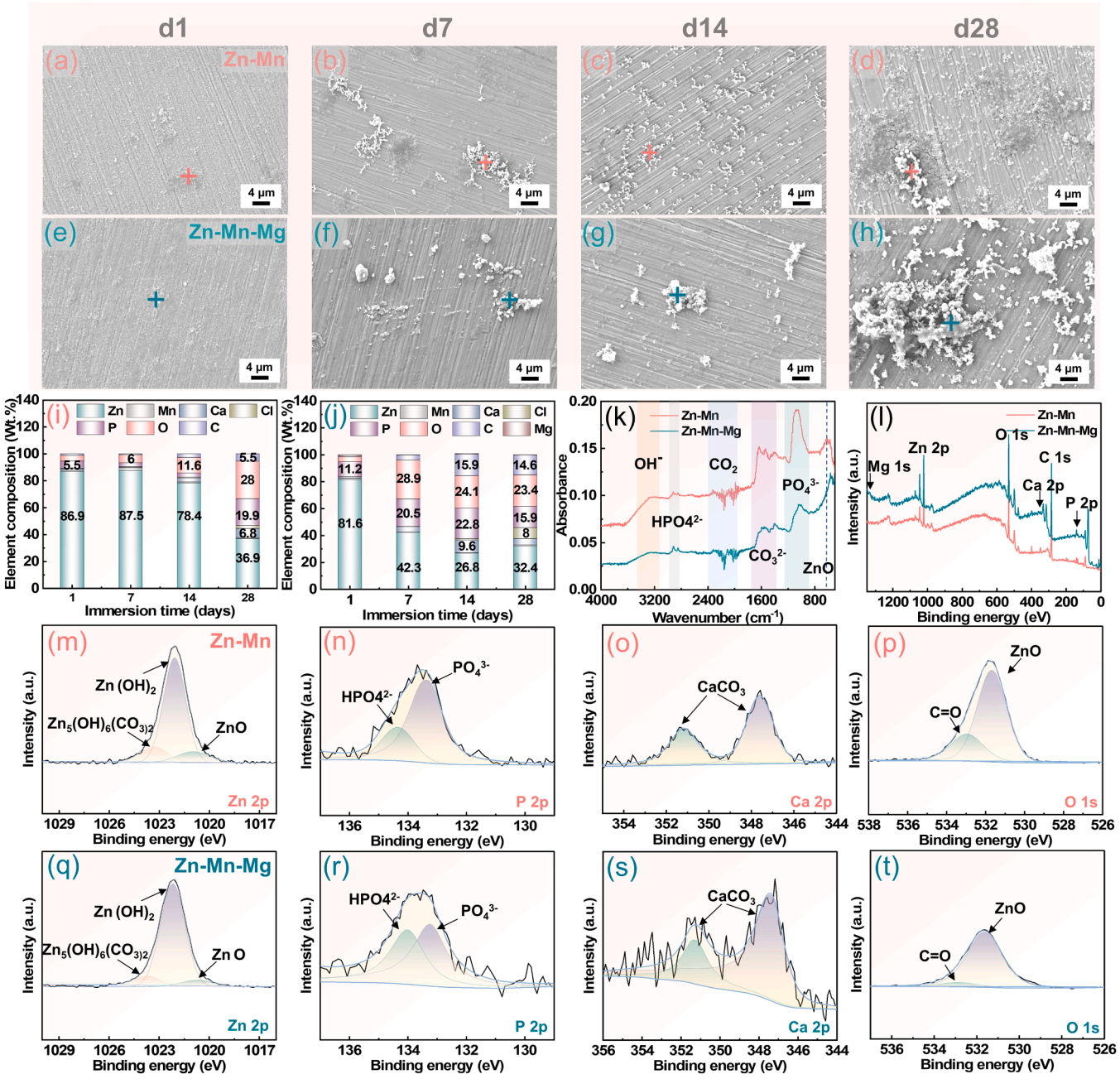

Fig. 6. *In vitro* biodegradation products analysis: (a–h) morphologies of the biodegradation products on the LPBF specimens at different immersion days, (i, j) compositions of the biodegradation products on the LPBF Zn-Mn and Zn-Mn-Mg alloy specimens at various immersion days, respectively, (k) FTIR spectra of the biodegradation products after immersion in the SBF for 28 days, (l) XPS full spectra of the biodegradation products on the LPBF Zn-Mn and Zn-Mn-Mg alloy specimens after immersion in the SBF for 28 days, and (m–t) high-resolution spectra of the Zn-2p, P-2p, Ca-2p and O-1s peaks collected from the biodegradation products after immersion in the SBF for 28 days.

immersion time points (Fig. 5i) according to Eq. (1). As the immersion time increased, the biodegradation rates of the Zn-Mn and Zn-Mn-Mg alloy specimens decreased from 0.55 mm/y and 0.46 mm/y on day 1 to 0.15 mm/y and 0.14 mm/y on day 28, respectively.

On day 1, the surfaces of the Zn-Mn and Zn-Mn-Mg alloy specimens exhibited almost no visible biodegradation products (Fig. 6a and e). From day 7 to day 28, however, white biodegradation products gradually appeared, especially on the Zn-Mn alloy specimens (Fig. 6b–d and f–h). The biodegradation products on the Zn-Mn alloy specimens were smaller in size and more uniformly distributed (Fig. 6c and d). In contrast, they appeared in the form of clusters on the Zn-Mn-Mg alloy specimens at the same time intervals (Fig. 6g and h). After removing the corrosion products (28 days) from the surface of the Zn-Mn-Mg alloy specimen (Fig. S2), localized corrosion pits (marked by the white arrows) were clearly visible, whereas the Zn-Mn alloy specimen showed an almost pit-free surface.

EDS analysis revealed that the biodegradation products mainly comprised Zn, Mn, Mg, O, Ca, P, Cl, and C elements (Fig. 6i and j). As the immersion time increased, the Zn content of the biodegradation products gradually decreased while the O and Ca contents increased. FTIR identified ZnO, PO_4^{3-}, CO_3^{2-}, HPO_4^{2-}, and OH^- signals on the surfaces of both types of specimens after 28 days of immersion (Fig. 6k). XPS wide scan spectra confirmed the compositions of the biodegradation products (Fig. 6l), with high-resolution spectra of Zn-2p, P-2p, Ca-2p, and O-1s peaks revealing the presence of ZnO, $Zn(OH)_2$, $Zn_5(OH)_6(CO_3)_2$, $CaCO_3$, PO_4^{3-}, and HPO_4^{2-}(Fig. 6m–t).

3.5. *In vitro* cytocompatibility

Live/dead staining showed that most MC3T3-E1 cells were alive (green fluorescence) after 1 day of culture in the 10 %, 20 %, and 50 % diluted extracts from both materials (Fig. 7). The cell density and morphology closely resembled those of the negative control group cultured with α-MEM (Fig. 7a5 and b5). The numbers of viable cells in these extracts were significantly larger compared to the positive control (DMSO) (Fig. 7a6 and b6), where few viable cells were observed. In

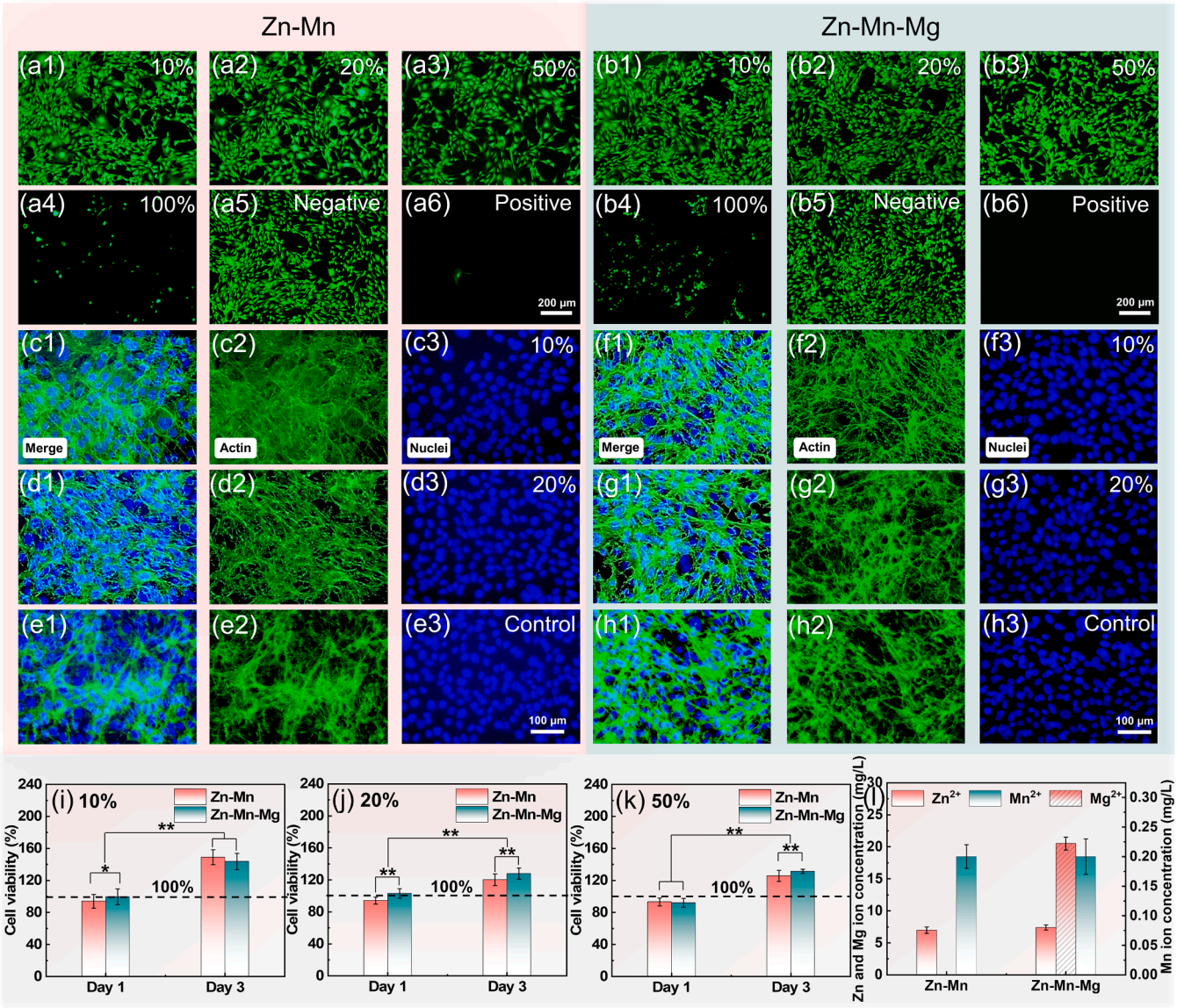

Fig. 7. Assessment of cytocompatibility *in vitro*: (a, b) live/dead staining images of the MC3T3-E1 cells cultured with the 10 %-, 20 %-, 50 %-, and 100 %-diluted extracts from the LPBF Zn-Mn and Zn-Mn-Mg alloy specimens for 1 day, (c–e) fluorescence microscope images of the MC3T3-E1 cells cultured with the Zn-Mn alloy specimen extracts with and without dilution, (f–h) fluorescence microscope images of the MC3T3-E1 cells cultured with the Zn-Mn-Mg alloy specimen extracts with and without dilution (the actin cytoskeleton was stained green and the nuclei were stained blue), (i–k) viability of the MC3T3-E1 cells cultured with the 10 %-, 20 %- and 50 %-diluted extracts for 1 day and 3 days, respectively, (l) Zn^{2+}, Mn^{2+}, and Mg^{2+} ion concentrations in the 100 % extracts.

contrast, a few cells survived in the 100 % extracts from both materials (Fig. 7a4 and b4). Cells cultured with the 10 % and 20 % extracts were well spread and exhibited cytoplasmic filament formation after 1 day (Fig. 7c–h).

The CCK8 assay (Fig. 7i–k) quantitatively assessed cell viability at different extract concentrations. The cell viability was about 100 % after 1 day of culture with the 10 %- 20 %- and 50 %-diluted extracts from both materials. By day 3, cell proliferation continued, with cell viability exceeding 120 %. No significant differences were observed in cell viability between the Zn-Mn and Zn-Mn-Mg extracts after either 1 day or 3 days of culture. The concentrations of the released Zn and Mn ions were similar in the 100 % extracts from both materials, while the concentration of Mg ions in the Zn-Mn-Mg extract was nearly twice as much as that of Zn ions (the Mg ion concentration in the medium was about 16 mg/L) (Fig. 7l).

ALP staining showed that the cells with the 10 %-diluted extract were slightly darker than those with the 20 %-diluted extract or the control groups after 14 days. However, there was no significant difference in the ALP activity between the same concentration extracts from the Zn-Mn and Zn-Mn-Mg alloy specimens (Fig. 8a–f). Compared to the control group, both Zn-Mn and Zn-Mn-Mg groups showed significantly higher mRNA expression levels of the osteogenic markers. Notably, the Zn-Mn-Mg group exhibited higher RUNX2, COL1, and OCN expression levels than the Zn-Mn group (Fig. 8g–i).

4. Discussion

In this study, we designed the Zn-Mn binary alloy and Zn-Mn-Mg ternary alloy and used LPBF to create fine microstructures to enhance Zn's strength and ductility. The additions of Mn and Mg to Zn led to the formation of significantly refined grains during LPBF without post-processing, for example, by applying hot isostatic pressing (HIP), or involving any plastic deformation as in the conventional material processing routes [4–6]. In the ternary alloy, the $MnZn_{13}$ and Mg_2Zn_{11} second phases formed inside the grains and along the grain boundaries, stimulating recrystallization and effectively restraining grain growth. As a result, we, for the first time, achieved a superior balance of strength and ductility in AM biodegradable Zn alloys, meeting the requirements of mechanical properties for bone fixation and substitution devices. These two alloys exhibited moderate biodegradation rates and favorable biocompatibility. The results obtained suggested that the AM biodegradable Zn-Mn-Mg alloy holds huge potential as a bone repair material, particularly for load-bearing orthopedic applications.

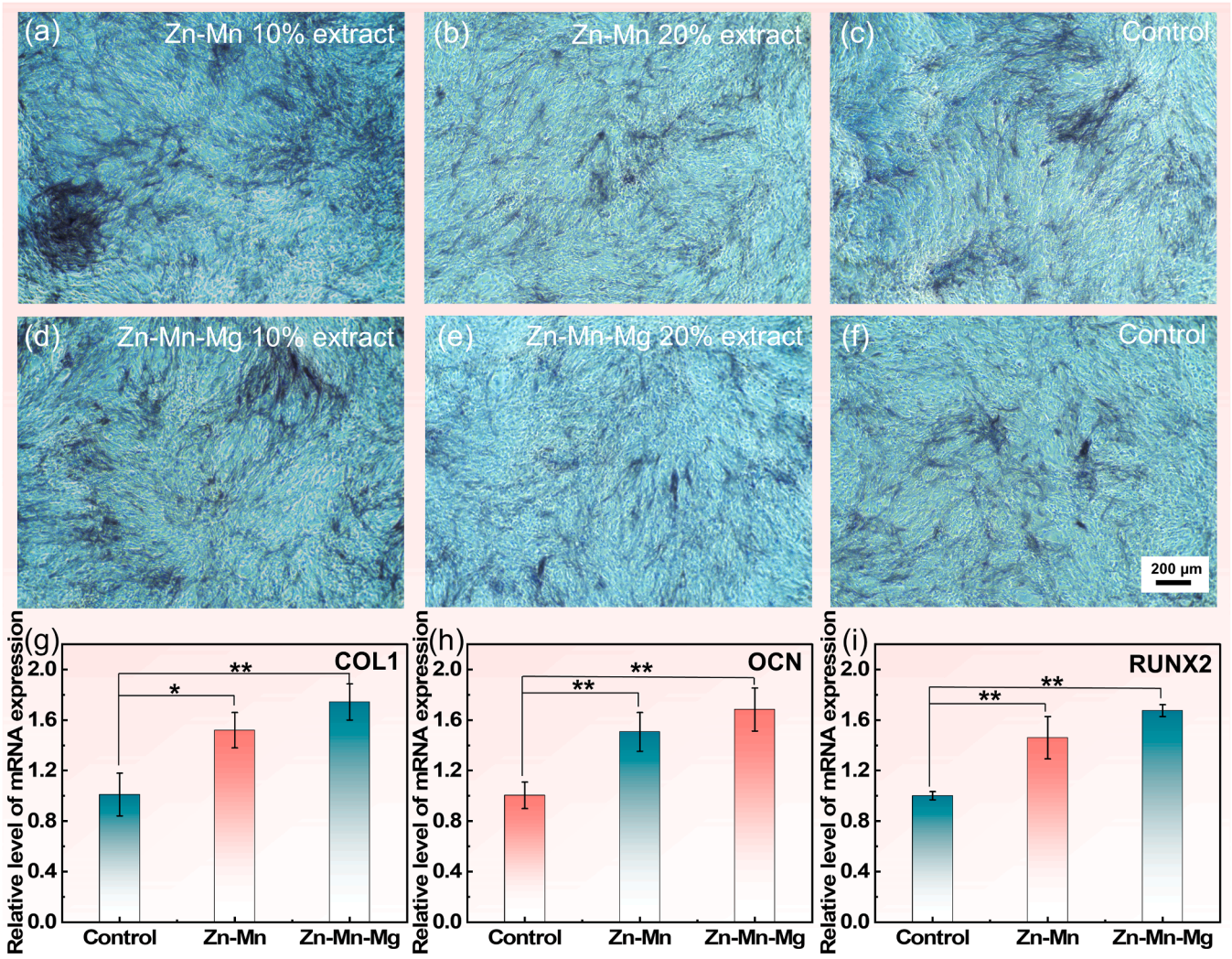

Fig. 8. Assessment of osteogenic ability *in vitro*: (a–f) ALP activities of the MC3T3-E1 cells cultured with the 10 %- and 20 %-diluted extracts for 14 days, (g–i) relative expression levels of osteogenesis-related genes (COL1, OCN, and RUNX2) with the 10 %-diluted extracts after 14 days, determined by performing the RT-PCR analysis.

4.1. Unique microstructure and superior balance of strength and ductility

The LPBF Zn-Mn-Mg alloy demonstrated an exceptional balance between strength and ductility, when compared to the mechanical properties of Zn-based materials reported in the literature [12–14,16,17,22,32–36] (Fig. 9b). The enhanced mechanical properties and their balance are closely related to the unique microstructure of the ternary alloy. Based on the detailed microstructural analysis, we constructed a schematic diagram illustrating the dual-phase strengthening mechanisms operating both inside the grains and at the grain boundaries (Fig. 9a).

During LPBF, the cooling rate can reach 10^6–10^7 K/s [37,38]. Given that the maximum solid solubility of Mn in Zn is about 0.8 % at the eutectic temperature (405 °C) [39], the majority of Mn would be entrapped in a supersaturated solid solution within the Zn matrix instead of precipitating immediately, as a result of the extension of the solubility limit. Upon solidification, some Mn could participate in the formation of the particulate $MnZn_{13}$ phase that was mostly distributed along the grain boundaries with the zone axis of Zn [0001] // $MnZn_{13}$ [110] (Fig. 3a, l and s). In a previous study, a similar $MnZn_{13}$ phase distributed along the grain boundaries and within grains was observed in the multi-pass cold-drawn Zn-0.5Mn alloy [40], but no acicular phase was found in their study. In the present study, due to the layer-by-layer nature of the manufacturing method used, the already dissolved Mn could precipitate from the Zn matrix when the laser beam reheated or even remelted the preceding layer. This phenomenon is known as heat history-induced precipitation or LPBF-fabricated *in-situ* precipitation [41,42], akin to the aging process commonly applied to precipitation-hardening alloys. The acicular and particulate second phases were dispersed inside the grains and at the grain boundaries, providing effective strengthening effects. As evidenced by the results of the tensile tests, the UTS of the Zn-Mn binary alloy was about 190 MPa, which is much higher than that of pure Zn [11,16,17]. However, the strengthening effect provided by the $MnZn_{13}$ phase could have been even stronger if the alloy had not fractured before the yielding point [21,22]. The highly limited plasticity of the Zn-Mn binary alloy could be related to its grain sizes, with an average grain size of about 35 μm and columnar morphology (Fig. 2l). Moreover, the strains near the columnar grain edges were markedly higher than those inside the grains (Fig. 2o), leading to an uneven stress distribution, which would hinder uniform plastic deformation during tensile testing. The hardness of the Zn-Mn alloy and Zn-Mn-Mg specimens exhibited no clear differences (p = 0.14) (Fig. 4f), similar to the results of CYS (p = 0.75) (Fig. 4e).

When a small amount of Mg was added to the Zn-1.0Mn alloy, both strength and plasticity significantly improved, surpassing all other AM biodegradable zinc alloys and Zn-matrix composites reported in the literature (Fig. 9b). The addition of Mg to the Zn-Mn alloy led to further refinement of grains by > 10 folds, manifested as a significant reduction in the average grain size down to 2.8 μm. The ultrafine Zn grains could play a coordinating role in uniform plastic deformation [21]. As deformation progressed during the tensile tests, dislocation multiplication occurred in the Zn matrix region adjacent to the hard particulate second phases (*i.e.*, $MnZn_{13}$ and Mg_2Zn_{11} in the present ternary alloy). These dislocations could propagate into the barren area of the Zn matrix without the particulate second phases where deformation energy could be accommodated, thereby effectively delaying stress concentration and preventing premature fracture, leading to uniform plastic deformation in the macroscale [43]. Moreover, during LPBF, excessive Mg in the Zn matrix precipitated out to form another second phase (Mg_2Zn_{11}), which was mainly distributed along the grain boundaries and arranged alternately with $MnZn_{13}$, further enhancing the grain boundary strengthening effect (Fig. 3j–l). As a combined result, the UTS of the Zn-Mn-Mg ternary alloy reached 290 MPa.

The impressive balance of the LPBF Zn-Mn-Mg alloy between strength and plasticity stems from the synergistic interactions between Zn, Mn, and Mg. While both the LPBF Zn-1Mn (this paper) and Zn-3Mg [19] binary alloys had similarly poor elongation values despite promising compressive strengths, their microstructures and strengthening

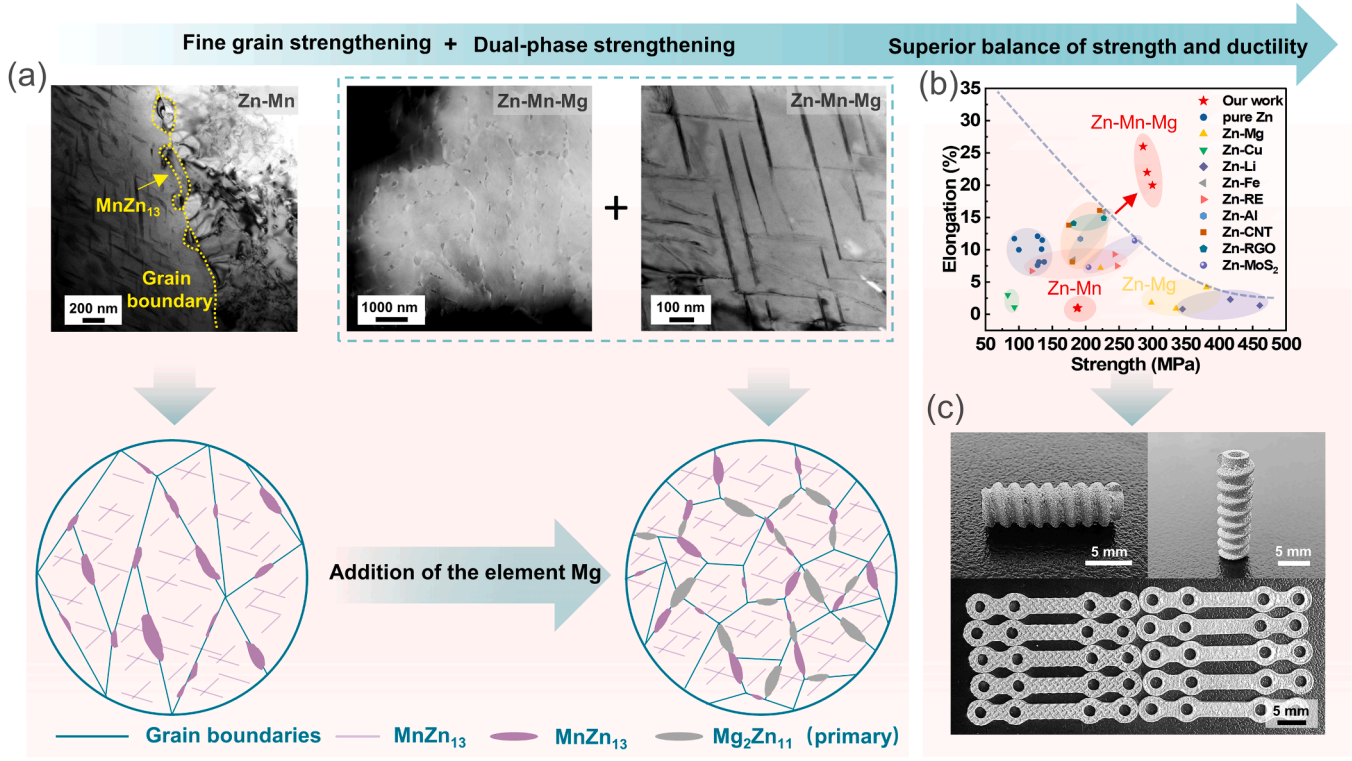

Fig. 9. (a) schematic diagram of the dual-phase synthetic strengthening mechanism, (b) ultimate tensile strength *versus* elongation – data collected from the current work and other literature [12–14,16,17,22,32–35,89], and (c) LPBF Zn-Mn-Mg bone screws and bone plates.

mechanisms differed significantly. Unlike the columnar grains and stress concentrations found in the LPBF Zn-1Mn binary alloy, the LPBF Zn-3Mg binary alloy had fine, uniform equiaxial grains. In the LPBF Zn-3Mg alloy, the mismatch in stiffness between the hard, brittle eutectic phases and the soft Zn matrix led to the occurrence of cracks at the interface of the eutectic structure, leading to premature fracture during deformation similar to its cast counterpart [44]. In contrast, the present Zn-Mn-Mg ternary alloy not only had refined grains but also benefited from the combined strengthening effects of two types of second phases, which strengthened both the interior of the grains and the grain boundaries and enabled continuous and uniform plastic deformation (Fig. 9a). Typically, the following equation [45] can be used to calculate the yield strength (σ_y) of an alloy:

$$\sigma_y = \sigma_s + \sigma_{gb} + \sigma_p + \sigma_d \tag{2}$$

where σ_s represents solid solution strengthening, σ_{gb} represents grain boundary strengthening, σ_p and σ_d are the strengthening effects contributed by second phase and dislocations, respectively. According to the Zn-Mn phase diagram and Zn-Mg phase diagram [39], the solid solubilities of Mn and Mg in the Zn matrix are almost zero at room temperature, thus σ_s can be neglected. σ_{gb} can be calculated by using the Hall-Petch Equation [46]:

$$\sigma_{gb} = k_d d^{-\frac{1}{2}} \tag{3}$$

where k_d represents the strengthening coefficient (110 MPa·μm$^{1/2}$) [47], d is the is the average grain size (2.8 μm, Fig. 2m). σ_p is mainly controlled by the Orowan mechanism [48]. Since there are mainly two types of precipitated phases in this ternary alloy, it can be calculated as follows:

$$\sigma_p = \sigma_{granular} + \sigma_{acicular} \tag{4}$$

The strength contributions by the granular second phase and acicular second phase can be calculated by using the Eq. (5) [19] and (6) [48], respectively:

$$\sigma_{granular} = \frac{M\mu b}{L} \tag{5}$$

$$\sigma_{acicular} = \frac{0.13\mu b}{2\sqrt{rh}} \left[f_v^{\frac{1}{2}} + 0.75\left(\frac{r}{h}\right)^{\frac{1}{2}} f_v + 0.14\left(\frac{r}{h}\right) f_v^{\frac{3}{2}} \right] ln\left(\frac{0.079r}{r_0} \right) \tag{6}$$

where M (1.23, Fig. S3) represents Taylor factor, μ is the shear modulus (39.5 GPa) [49], b is the Burgers vector (0.266 nm) [50], and L is the average size of the granular precipitated phase particles (~250 nm, which is statistically obtained *via* Fig. 3j and k). r_0 represents the inner radius, it is generally considered to be equal to the Burgers vector [48], the r, h, f_v are the diameter, thickness and volume fraction of the acicular second phase, respectively. These data can be measured from Fig. 3j and k, where r, h, f_v are 40 nm, 4.5 nm, 0.04, respectively. Local internal stresses in the specimens can develop during the LPBF process due to rapid solidification. These stresses create the regions that impede dislocation movement during deformation, a phenomenon that can be described by the Bailey-Hirsch relation [51]:

$$\sigma_d = \alpha M b G \sqrt{\rho} \tag{7}$$

where α represents the dislocation interaction constant (0.2) [52], and ρ (~10^{14} m^{-2}, Fig. 2p) is the localized dislocation density obtained from the EBSD data. According to the above equations, σ_{gb}, $\sigma_{granular}$, $\sigma_{acicular}$ and σ_d are calculated to be 65.74 MPa, 51.7 MPa, 75 MPa and 25.8 MPa, respectively, and the sum of these values (218.2 MPa) closely matches the experimental value of 213.5 MPa.

Notably, although adding Mg significantly enhanced the strength and ductility of the Zn-Mn alloy, the LPBF process parameters used for fabricating the Zn-Mn and Zn-Mn-Mg alloy specimens differed. LPBF process parameters, such as scanning speed, indeed influence the microstructure and mechanical properties, as demonstrated in our previous study [19] and in other studies [13,53,54]. However, considering the fact that the Mg element plays a dominant role in refining Zn grains and forming a second phase, it is plausible that the alloy composition has a more significant impact than the process parameters [13]. For instance, when comparing the microstructures of the Zn-Mn-Mg alloy specimens fabricated at different scanning speeds, it appeared that while scanning speed affected grain morphology, it hardly influenced grain size (Fig. S4). Therefore, in this study, we focused on the effect of the alloying element Mg on the microstructure and mechanical properties.

The high strength and the superior balance between strength and ductility, achieved in the present research, enable the LPBF Zn-Mn-Mg ternary alloy to meet the design criteria for bone fixation devices (Fig. 9c) and stents [55]. Moreover, the dual-phase synthetic strengthening strategy formulated in this study opens up an additional chapter in the design of AM Zn alloys with optimized mechanical properties.

4.2. Biodegradation behavior

Modulating the biodegradation behavior of implants to be compatible with the bone remodeling process is important for its clinical application. Compared to the widely reported Mg alloys [56–58], Zn alloys display more suitable biodegradation rates. Complete bone regeneration usually requires 3–12 weeks for the upper limbs and 12–24 weeks for lower limbs [3]. During the initial 3–6 months of bone regeneration, implants need to maintain steady mechanical strength to support bone regeneration. Thereafter, they gradually degrade over a total period of 1–2 years. Generally, this requires a biodegradation rate of about 0.2–0.5 mm/year [59,60]. In this study, the 28-day biodegradation rates of the Zn-Mn and Zn-Mn-Mg alloys were around 0.15 mm/year. This is higher than the values of the Zn-Mn and Zn-Mn-Mg alloys prepared by conventional manufacturing techniques [4,23,61] and close to the ideal biodegradation rate for bone implants. For the Zn-Mn binary alloy, the corrosion occurs homogeneously, which can be attributed to the distribution and quantity of the second-phase particles. Additionally, the high residual stresses at the edges of the columnar grains (Fig. 2p) significantly influence the degradation behavior. These stresses alter the "free energy state" of the material, which accelerates its biodegradation [62]. In contrast, the Zn-Mn-Mg ternary alloy exhibits localized corrosion, which arises from the combined effects of grain size and micro-galvanic corrosion at the interfaces between the second phases (Mg_2Zn_{11} and $MnZn_{13}$) and the Zn matrix. Previous studies [63–65] have shown that a smaller grain size tends to decrease the biodegradation rate, while the presence of secondary phases, such as Mg_2Zn_{11} and $MnZn_{13}$ in the Zn-Mn-Mg alloy, can form micro-galvanic cells that accelerate biodegradation [62]. After removing the corrosion products from the surface of the Zn-Mn-Mg alloy specimen (Fig. S2), localized corrosion pits (marked by the white arrows) were clearly visible, confirming this effect. Furthermore, the Zn-Mn and Zn-Mn-Mg alloys with nearly full densities demonstrated slower biodegradation rates than the porous Zn alloy scaffolds that we previously reported [46,66], which could be attributed to the fact that porous scaffolds have a larger surface area and allow the penetration of the corrosive medium into the structure to accelerate biodegradation.

The biodegradation rates calculated from the electrochemical tests were higher than those from the immersion tests, as PDP accelerated biodegradation, mainly reflecting short-term biodegradation behavior. The fitting results (Table 3) of EIS revealed that the R_f and R_{ct} values of the Zn-Mn-Mg alloy were larger than those of the Zn-Mn alloy. However, the PDP analysis (Table 2) indicated that the biodegradation rate of the Zn-Mn-Mg ternary alloy was slightly higher than that of the Zn-Mn binary alloy. While EIS shows the behavior of the electrodes at equilibrium, PDP reflects the conditions in which the electrodes are subjected to strong polarization [67]. Therefore, a high impedance value may not directly indicate a low biodegradation rate [23,68].

The differences in the biodegradation behavior of both alloys led to the distinct characteristics of the biodegradation products in terms of morphology and distribution. The biodegradation products on the Zn-Mn alloy specimens were finer and more uniformly distributed, while those on the Zn-Mn-Mg alloy specimens appeared to cluster at different locations. This difference must be closely linked to the distinct microstructures of these two alloys. The Zn-Mn binary alloy consists mainly of large columnar grains, with a small proportion of Mn precipitated from the Zn matrix to form the fine acicular phase having only a 32 mV potential difference from the Zn matrix [4]. The alloy is, thus, less susceptible to micro-galvanic corrosion, resulting in uniform biodegradation. In contrast, the Zn-Mn-Mg alloy contained a large number of particulate precipitates along the grain boundaries, which exhibited significant differences in potential from the Zn matrix [4]. Moreover, the $MnZn_{13}$ and Mg_2Zn_{11} phases have a substantial potential difference (251 mV) [4], making the material more prone to micro-galvanic corrosion and localized biodegradation. Although Mg_2Zn_{11} was preferentially subjected to localized corrosion through micro-galvanic interactions with the matrix, it was uniformly distributed macroscopically in the specimen, as shown in Fig. S2. In the future, numerical models [69,70] as a cost-effective and efficient tool may be employed to simulate the long-term corrosion behavior of AM Zn alloy implants to aid in alloy and architectural design optimization.

The biodegradation products were mainly composed of ZnO, $Zn(OH)_2$, $Zn_5(OH)_6(CO_3)_2$, $CaCO_3$, PO_4^{3-}, and HPO_4^{2-}, which are similar to those of most zinc alloys, such as Zn-Mn alloys [40], Zn-Mg alloys [68] and Zn-Mg-Cu alloys [68]. Typically, zinc alloys degrade by the anodic oxidation of Zn to Zn^{2+} and the cathodic reduction of oxygen in the physiological environment, resulting in the formation of ZnO and $Zn(OH)_2$ passivation layers (Fig. 5). These passivation layers provide the Zn matrix with effective protection during biodegradation [71]. However, a large number of chloride ions in physiological media can destroy the passivation layers, converting them into soluble salts, such as zinc hydroxide chloride and zinc hydroxide phosphate [55,72]. Although these corrosion products may slightly increase the pH value in a physiological environment [11], it has been shown that appropriate concentrations of corrosion products do not adversely affect the surrounding tissues by disturbing the local physiological equilibrium at the implantation site [73,74]. Meanwhile, these soluble salts may also be absorbed by osteoclasts and induce osteogenesis by osteoblasts [75], but the mechanism is currently unclear and requires further study. While *in vitro* biodegradation experiments provide the first cues regarding how biodegradation might happen *in vivo*, separate sets of animal experiments or clinical trials are needed to evaluate the actual biodegradation behavior of the developed biomaterials *in vivo*.

4.3. Biocompatibility and osteogenic activity

The MC3T3-E1 cells were highly viable when cultured in the 10 %-, 20 %-, and 50 %-diluted extracts from the LPBF Zn-Mn and Zn-Mn-Mg alloy specimens at day 1 (Fig. 7). The cells proliferated from day 1 to day 3, indicating cytocompatibility. However, only a few viable cells were observed in the 100 % extracts (Fig. 7a4, b4), likely due to the ion concentrations exceeding the tolerance limits for the cells. Although the Mg^{2+} ion concentration was greater than the Zn^{2+} ion concentration in the 100 % extracts from the Zn-Mn-Mg alloy specimen, the toxicity threshold of the Mg^{2+} ion is much higher than that of the Zn^{2+} ion. Previous studies have shown that a Mg^{2+} ion concentration below 100 μg/mL does no harm cell viability, while concentrations exceeding 300 μg/mL can induce significant cell death [76]. In this study, the Mg^{2+} ion concentration in the 100 % extract from the Zn-Mn-Mg alloy specimen was approximately 4 μg/mL, well below the toxicity threshold. Mn, an essential trace element in the human body, serves as a coenzyme in various fundamental life processes, including energy metabolism, bone formation, and free radical scavenging. A previous study [77] has shown that a critical Mn^{2+} ion concentration is around 12.7 μg/mL above which Mn^{2+} ion tends to harm cell proliferation. In this work, the Mn^{2+} ion concentration in the 100 % extracts from both of the specimens was only about 0.2 μg/mL, well below the threshold value. Hence, the primary factor causing cell death is likely the Zn^{2+} ion concentration. Indeed, the Zn^{2+} ion concentration in the 100 % extracts from the specimens of both materials was about 7 μg/mL, which exceeded the optimum range for cell proliferation (0–3.9 μg/mL) [78]. However, *in vivo,* the biodegradation products can be metabolized or transported away, and therefore, a dilution of 9 to 14 times is recommended for evaluating the biocompatibility of biodegradable metals [79]. The 10 % dilution extract align with this recommendation, while the 20 % dilution extract and 50 % dilution extract provide harsher cell conditions. In the 50 %-diluted extracts, the Zn^{2+} ion concentration was around 3.5 μg/mL, being lower than the critical threshold (3.9 μg/mL). Therefore, the cells in the 50 %-diluted extracts showed high cell viability, according to the CCK8 quantitative analysis and live/dead staining results (Fig. 7).

ALP activity and gene expression tests were also performed to further explore the effects of manganese and magnesium on the osteogenic behavior of MC3T3-E1 cells. ALP, as an important early marker of osteogenesis, is typically used to detect the early osteogenic differentiation behavior of cells [68]. The ALP staining results indicated that the cells in the Zn-Mn and Zn-Mn-Mg groups stained darker than the control group, demonstrating that the cells in the experimental groups were well-differentiated in early osteogenesis (Fig. 8). Zinc has been reported to enhance ATPase activity and regulate the transcription of osteoblast differentiation-related genes such as ALP, osteopontin, osteocalcin, and type I collagen [74,80,81]. Furthermore, Zn is essential for promoting bone formation by activating protein synthesis in osteoblasts [74,82]. Extracellular Zn^{2+} ion promotes osteogenesis *via* endocytosis into bone marrow stromal cells (BMSC) and activation of the extracellular signal-regulated kinase (ERK) pathway [83]. This osteogenic effect was confirmed by the quantitative results of the late markers for osteogenesis, such as COL 1, OCN, and RUNX 2 (Fig. 8g–i). The mRNA expression levels in the Zn-Mn-Mg group were higher than those in the Zn-Mn group, which could be attributed to the beneficial effect of the Mg^{2+} ion. It is well known that Mg^{2+} ion is widely distributed in bone and can promote local Ca^{2+} ion deposition and bone tissue growth by antagonizing Ca^{2+} ions [84]. Mg deficiency may cause osteoporosis. Therefore, calcium and magnesium supplementation are often required. A moderate amount of Mg^{2+} ion not only enhances osteoblast activity *via* promoting adhesion and proliferation of cells as well as increasing the bone tissue collagen content and stimulating vascular endothelial growth factor release, which further enhance bone tissue regeneration [85,86].

4.4. Limitations and future work

Although we successfully prepared two Zn alloys *via* LPBF and achieved a superior balance of strength and ductility in the case of the Zn-Mn-Mg ternary alloy, moderate biodegradation rates, and acceptable biocompatibility, several key areas require further exploration. First, only MC3T3-E1 murine cell line was used for the static biodegradation tests. Expanding the study to include responses of other cell lines in a dynamic bioreactor would indeed offer valuable insights into the biocompatibility and potential interactions of the LPBF Zn-Mn-Mg alloy under more physiologically relevant conditions. This approach could better simulate the *in vivo* environment and provide a broader understanding of cell-material interactions and degradation effects over time. Considering the differences between *in vitro* and *in vivo* environments, animal tests are essential to validate the biocompatibility, osteogenic effects, and biodegradation behavior of the materials under physiological conditions. Second, this study focused on the properties of bulk materials. Future research should investigate porous Zn-Mn-Mg alloy scaffolds for the critical-size bone defect regeneration. Third, considering the cyclic loading that most bone fixation devices are subjected to, corrosion fatigue tests are needed to understand the behavior of the

material under dynamic conditions. Finally, considering the significant differences in processing conditions between AM and conventional formative or subtractive manufacturing, biodegradable alloy compositions should be specifically tailored for AM, considering the rapid solidification involved in laser-based AM. Apart from the processing conditions, loading conditions may also influence the mechanical properties. For instance, Jin [87] and Chen [88] et al. observed that zinc alloys exhibited significantly different mechanical properties at different loading rates. A Higher strain rate led to an increased dislocation density and tensile strength but reduced elongation [87]. This was attributed to an increased difficulty of plastic deformation, limited uniform dislocation propagation, and a mismatch between dislocation movement and loading rate, resulting in earlier fracture. The loading rate used in this study was 0.001 s^{-1}, meeting the requirements of ISO 6892–1:2019. While the strain rate sensitivity of LPBF Zn alloys under dynamic loading conditions remains unexplored, it is a highly interesting area for future research.

5. Conclusions

A Zn-Mn-Mg ternary alloy with an extraordinary balance of strength and ductility has been successfully prepared using LPBF. This is the first instance of a directly printed biodegradable alloy meeting the mechanical property requirements for bone fixation devices, such as bone screws or plates, without the need for post-processing. Moreover, both the binary and ternary alloys showed moderate biodegradation rates and favorable biocompatibility *in vitro*, paving the way for their further investigations toward clinical adoption, especially for load-bearing orthopedic applications.

The LPBF Zn-Mn-Mg ternary alloy showed an ultimate tensile strength of 289 MPa, a yield strength of 213.5 MPa, and elongation exceeding 20 %. The superior balance of strength and ductility could be attributed to the unique microstructure resulting from the addition of Zn, Mn, and Mg. The distributions of $MnZn_{13}$ and Mg_2Zn_{11} second phases inside the grains and at the grain boundaries contributed to dual-phase synthetic strengthening, resulting in high strength values. The significant refinement of the Zn grains by adding Mg to the Zn-Mn alloy facilitated uniform plastic deformation, resulting in high elongation.

LPBF Zn-Mn and Zn-Mn-Mg alloys exhibited biodegradation rates around 0.15 mm/year, close to the desired range (0.2–0.5 mm/year) for bone fixation devices. The corrosion mechanisms, however, differed due to the differences in microstructure. The Zn-Mn binary alloy primarily underwent uniform biodegradation due to its larger average grain size and less precipitated second phase. In contrast, the Zn-Mn-Mg alloy exhibited localized biodegradation caused by galvanic corrosion between the precipitates and the Zn matrix.

The developed alloys also showed $>$ 85 % viability of the MC3T3-E1 cells in the 10 %-, 20 %-, and 50 %-diluted extracts, as confirmed by the CCK8 assay, live/dead staining, and cytoskeleton imaging. Moreover, the Zn alloys upregulated multiple osteogenic markers, attributed to the beneficial effect of the Mn and Mg alloying elements.

CRediT authorship contribution statement

Chengcong Huang: Writing – original draft, Methodology, Investigation, Data curation. **Yizhu Wang:** Methodology, Data curation. **Fan Yang:** Methodology, Data curation. **Yixuan Shi:** Investigation, Data curation. **Shangyan Zhao:** Methodology, Investigation. **Xuan Li:** Methodology, Investigation. **Yuchen Lu:** Software. **Yuzhi Wu:** Investigation, Data curation. **Jie Zhou:** Writing – review & editing, Writing – original draft, Methodology. **Amir A. Zadpoor:** Writing – review & editing, Writing – original draft, Methodology. **Wei Xu:** Writing – review & editing, Writing – original draft. **Yageng Li:** Writing – review & editing, Writing – original draft, Supervision, Resources, Project administration, Funding acquisition. **Luning Wang:** Writing – review & editing, Writing – original draft, Supervision, Project administration, Funding acquisition.

Declaration of competing interest

The authors declare that they have no known competing financial interests or personal relationships that could have appeared to influence the work reported in this paper.

Acknowledgments

The work was financially supported by the National Key Research & Development Program of China (No. 2023YFB3813000), the National Natural Science Foundation of China (52471260, 52201294, 52231010, 52071028, 52105421), Natural Science Foundation of Beijing (L212014), and Beijing Nova Program (2022 Beijing Nova Program Cross Cooperation Program No. 20220484178).

Supplementary materials

Supplementary material associated with this article can be found, in the online version, at doi:10.1016/j.actbio.2025.02.047.

References

[1] Y.G. Li, H. Jahr, J. Zhou, A.A. Zadpoor, Additively manufactured biodegradable porous metals, Acta Biomater. 115 (2020) 29–50.
[2] Y.G. Li, Y.X. Shi, Y.C. Lu, X. Li, J. Zhou, A.A. Zadpoor, L.N. Wang, Additive manufacturing of vascular stents, Acta Biomater. 167 (2023) 16–37.
[3] Y.F. Zheng, X.N. Gu, F. Witte, Biodegradable metals, Mater. Sci. Eng. R Rep. 77 (2014) 1–34.
[4] Z.Z. Shi, X.M. Li, S.L. Yao, Y.Z. Tang, X.J. Ji, Q. Wang, X.X. Gao, L.N. Wang, 300 MPa grade biodegradable high-strength ductile low-alloy (BHSDLA) Zn-Mn-Mg alloys: an *in vitro* study, J. Mater. Sci. Technol. 138 (2023) 233–244.
[5] H.T. Yang, B. Jia, Z.C. Zhang, X.H. Qu, G.N. Li, W.J. Lin, D.H. Zhu, K.R. Dai, Y. F. Zheng, Alloying design of biodegradable zinc as promising bone implants for load-bearing applications, Nat. Commun. 11 (1) (2020).
[6] M. Watroba, W. Bednarczyk, J. Kawalko, P. Bala, Fine-tuning of mechanical properties in a Zn-Ag-Mg alloy via cold plastic deformation process and post-deformation annealing, Bioact. Mater. 6 (10) (2021) 3424–3436.
[7] Y. Li, P. Pavanram, J. Bühring, S. Rütten, K.U. Schröder, J. Zhou, T. Pufe, L. N. Wang, A.A. Zadpoor, H. Jahr, Physiomimetic biocompatibility evaluation of directly printed degradable porous iron implants using various cell types, Acta Biomater. 169 (2023) 589–604.
[8] M. Montani, A.G. Demir, E. Mostaed, M. Vedani, B. Previtali, Processability of pure Zn and pure Fe by SLM for biodegradable metallic implant manufacturing, Rapid Prototyp. J. 23 (3) (2017) 514–523.
[9] P. Wen, Y. Qin, Y. Chen, M. Voshage, L. Jauer, R. Poprawe, J.H. Schleifenbaum, Laser additive manufacturing of Zn porous scaffolds: shielding gas flow, surface quality and densification, J. Mater. Sci. Technol. 35 (2) (2019) 368–376.
[10] S.L. Wu, X.M. Liu, K.W.K. Yeung, C.S. Liu, X.J. Yang, Biomimetic porous scaffolds for bone tissue engineering, Mater. Sci. Eng. R Rep. 80 (2014) 1–36.
[11] Y. Li, P. Pavanram, J. Zhou, K. Lietaert, P. Taheri, W. Li, H. San, M.A. Leeflang, J. M.C. Mol, H. Jahr, A.A. Zadpoor, Additively manufactured biodegradable porous zinc, Acta Biomater. 101 (2020) 609–623.
[12] Y. Qin, H. Yang, A. Liu, J. Dai, P. Wen, Y. Zheng, Y. Tian, S. Li, X. Wang, Processing optimization, mechanical properties, corrosion behavior and cytocompatibility of additively manufactured Zn-0.7Li biodegradable metals, Acta Biomater. 142 (2022) 388–401.
[13] M. Waqas, D. He, X. Wu, Z. Tan, W. Shao, X. Guo, Investigation on the preparation, microstructure, mechanical and degradation properties of laser additive manufactured Zn–Li–Mg alloy for bioresorbable application, J. Mater. Res. Technol. 26 (2023) 8509–8526.
[14] A. Liu, Y. Lu, J. Dai, P. Wen, D. Xia, Y. Zheng, Mechanical properties, *in vitro* biodegradable behavior, biocompatibility and osteogenic ability of additively manufactured Zn-0.8Li-0.1Mg alloy scaffolds, Biomater. Adv. 153 (2023) 213571.
[15] J. Venezuela, M.S. Dargusch, The influence of alloying and fabrication techniques on the mechanical properties, biodegradability and biocompatibility of zinc: a comprehensive review, Acta Biomater. 87 (2019) 1–40.
[16] Z. Dong, C. Han, Y. Zhao, J. Huang, C. Ling, G. Hu, Y. Wang, D. Wang, C. Song, Y. Yang, Role of heterogenous microstructure and deformation behavior in achieving superior strength-ductility synergy in zinc fabricated via laser powder bed fusion, Int. J. Extreme Manuf. 6 (4) (2024) 045003.
[17] J. Cui, L. Chao, J. Ren, C. Ling, D. Xie, D. Wang, H. Liang, H. Liang, Y. Yang, Microstructure development of AM-fabricated pure Zn with heat-treatment and its mechanical properties, degradation behavior, and biocompatibility, J. Mater. Res. Technol. 28 (2024) 3707–3721.
[18] Z. Dong, C. Han, G. Liu, J. Zhang, Q. Li, Y. Zhao, H. Wu, Y. Yang, J. Wang, Revealing anisotropic mechanisms in mechanical and degradation properties of

zinc fabricated by laser powder bed fusion additive manufacturing, J. Mater. Sci. Technol. 214 (2025) 87–104.
[19] Y. Zheng, C. Huang, Y. Li, J. Gao, Y. Yang, S. Zhao, H. Che, Y. Yang, S. Yao, W. Li, J. Zhou, A.A. Zadpoor, L. Wang, Mimicking the mechanical properties of cortical bone with an additively manufactured biodegradable Zn-3Mg alloy, Acta Biomater. 182 (2024) 139–155.
[20] P.S. Guo, F.X. Li, L.J. Yang, R. Bagheri, Q.K. Zhang, B.Q. Li, K. Cho, Z.L. Song, W. S. Sun, H.N. Liu, Ultra-fine-grained Zn-0.5Mn alloy processed by multi-pass hot extrusion: grain refinement mechanism and room-temperature superplasticity, Mater. Sci. Eng. A Struct. Mater. Prop. Microstruct. Process. 748 (2019) 262–266.
[21] Z.Z. Shi, J. Yu, X.F. Liu, Microalloyed Zn-Mn alloys: from extremely brittle to extraordinarily ductile at room temperature, Mater. Des. 144 (2018) 343–352.
[22] C. Shuai, S. Zhong, Z. Dong, C. He, Y. Shuai, W. Yang, S. Peng, Peritectic-eutectic transformation of intermetallic in Zn alloy: effects of Mn on the microstructure, strength and ductility, Mater. Charact. 190 (2022) 112054.
[23] B. Jia, H. Yang, Y. Han, Z. Zhang, X. Qu, Y. Zhuang, Q. Wu, Y. Zheng, K. Dai, *In vitro* and *in vivo* studies of Zn-Mn biodegradable metals designed for orthopedic applications, Acta Biomater. 108 (2020) 358–372.
[24] H.S. Jiang, X.G. Qiao, C. Xu, S. Kamado, K. Wu, M.Y. Zheng, Influence of size and distribution of W phase on strength and ductility of high strength Mg-5.1Zn-3.2Y-0.4Zr-0.4Ca alloy processed by indirect extrusion, J. Mater. Sci. Technol. 34 (2) (2018) 277–283.
[25] M. Luqman, Y. Ali, M.M.Y. Zaghloul, F.A. Sheikh, V. Chan, A. Abdal-hay, Grain refinement mechanism and its effect on mechanical properties and biodegradation behaviors of Zn alloys – A review, J. Mater. Res. Technol. 24 (2023) 7338–7365.
[26] L. Zhao, L. Song, J.G. Santos Macías, Y. Zhu, M. Huang, A. Simar, Z. Li, Review on the correlation between microstructure and mechanical performance for laser powder bed fusion AlSi10Mg, Addit. Manuf. 56 (2022) 102914.
[27] N. Li, T. Wang, L. Zhang, L. Zhang, Crack initiation mechanism of laser powder bed fusion additive manufactured Al-Zn-Mg-Cu alloy, Mater. Charact. 195 (2023) 112415.
[28] Y. Zhang, J. Xu, Y.C. Ruan, M.K. Yu, M. O'Laughlin, H. Wise, D. Chen, L. Tian, D. Shi, J. Wang, S. Chen, J.Q. Feng, D.H. Chow, X. Xie, L. Zheng, L. Huang, S. Huang, K. Leung, N. Lu, L. Zhao, H. Li, D. Zhao, X. Guo, K. Chan, F. Witte, H. C. Chan, Y. Zheng, L. Qin, Implant-derived magnesium induces local neuronal production of CGRP to improve bone-fracture healing in rats, Nat. Med. 22 (10) (2016) 1160–1169.
[29] J. Wang, J. Xu, B. Song, D.H. Chow, P. Shu-Hang Yung, L. Qin, Magnesium (Mg) based interference screws developed for promoting tendon graft incorporation in bone tunnel in rabbits, Acta Biomater. 63 (2017) 393–410.
[30] P. Cheng, P. Han, C. Zhao, S. Zhang, H. Wu, J. Ni, P. Hou, Y. Zhang, J. Liu, H. Xu, S. Liu, X. Zhang, Y. Zheng, Y. Chai, High-purity magnesium interference screws promote fibrocartilaginous entheses regeneration in the anterior cruciate ligament reconstruction rabbit model via accumulation of BMP-2 and VEGF, Biomaterials 81 (2016) 14–26.
[31] ASTM G31-72, Standard practice for laboratory immersion corrosion testing of metals. Annual Book of ASTM Standards, American Society for Testing and Materials, Filadelfia, Pennsylvania, 2004.
[32] C. Shuai, J. Zhang, Y. Yang, H. Qian, M. Yang, L. Yang, Epitaxial growth of rare-earth yttrium on nanosheets to form semicoherent interface in zinc implant, J. Mater. Res. Technol. 29 (2024) 1206–1217.
[33] Y. Yang, Y. Cheng, M. Yang, G. Qian, S. Peng, F. Qi, C. Shuai, Semicoherent interface strengthens graphene/zinc scaffolds, Mater. Today Nano 17 (2022) 100163.
[34] C. Shuai, Z. Dong, W. Yang, C. He, Y. Yang, S. Peng, Rivet-inspired modification of carbon nanotubes by *in situ*-reduced Ag nanoparticles to enhance the strength and ductility of Zn implants, ACS Biomater. Sci. Eng. 7 (12) (2021) 5484–5496.
[35] F. Meng, Y. Du, Research progress on laser powder bed fusion additive manufacturing of zinc alloys, Materials 17 (2024) 4309.
[36] Y. Zhou, J. Wang, Y. Yang, M. Yang, H. Zheng, D. Xie, D. Wang, L. Shen, Laser additive manufacturing of zinc targeting for biomedical application, Int. J. Bioprint. 8 (1) (2022) 1–22.
[37] D. Herzog, V. Seyda, E. Wycisk, C. Emmelmann, Additive manufacturing of metals, Acta Mater. 117 (2016) 371–392.
[38] D. Gu, Y.C. Hagedorn, W. Meiners, G. Meng, R.J.S. Batista, K. Wissenbach, R. Poprawe, Densification behavior, microstructure evolution, and wear performance of selective laser melting processed commercially pure titanium, Acta Mater. 60 (9) (2012) 3849–3860.
[39] E. Mostaed, M. Sikora-Jasinska, J.W. Drelich, M. Vedani, Zinc-based alloys for degradable vascular scent applications, Acta Biomater. 71 (2018) 1–23.
[40] P.S. Guo, X.L. Zhu, L.J. Yang, L. Deng, Q.K. Zhang, B.Q. Li, K. Cho, W.S. Sun, T. T. Ren, Z.L. Song, Ultrafine- and uniform-grained biodegradable Zn-0.5Mn alloy: grain refinement mechanism, corrosion behavior, and biocompatibility *in vivo*, Mater. Sci. Eng. C Mater. Biol. Appl. 118 (2021) 111391.
[41] H. Zhang, Y. Wu, Y. Wang, W. Deng, G. Xu, K. Luo, J. Lu, *In-situ* nanoscale precipitation behavior and strengthening mechanism of WC/IN718 composites manufactured by laser powder bed fusion, Compos. Part B Eng. 284 (2024) 111727.
[42] J. Liang, S. Wu, Z. Lei, Y. Chen, X. Zhang, B. Li, M. Jiang, Y. Chen, *In-situ* aging treatment by preheating to obtain high-strength ZK60 Mg alloy processed by laser powder bed fusion, Mater. Charact. 194 (2022) 112361.
[43] Y. Wu, Q. Fu, B. Guo, W. Chen, X. Xiao, W. Li, Z. Yu, Revealing the mechanical and degradation properties of the Zn-Cu-Ti alloy with ununiform heterostructure, Mater. Sci. Eng. A Struct. Mater. Prop. Microstruct. Process. 853 (2022) 143775.
[44] L. Ye, H. Huang, C. Sun, X. Zhuo, Q. Dong, H. Liu, J. Ju, F. Xue, J. Bai, J. Jiang, Effect of grain size and volume fraction of eutectic structure on mechanical properties and corrosion behavior of as-cast Zn–Mg binary alloys, J. Mater. Res. Technol. 16 (2022) 1673–1685.
[45] L.Q. Wang, Y.P. Ren, S.N. Sun, H. Zhao, S. Li, G.W. Qin, Microstructure, mechanical properties and fracture behavior of as-extruded Zn-Mg binary alloys, Acta Metall. Sin. English Letters 30 (10) (2017) 931–940.
[46] Y. Li, P. Pavanram, J. Zhou, K. Lietaert, F.S.L. Bobbert, Y. Kubo, M.A. Leeflang, H. Jahr, A.A. Zadpoor, Additively manufactured functionally graded biodegradable porous zinc, Biomater. Sci. 8 (9) (2020) 2404–2419.
[47] D.S. Liang, C.X. Wei, F.Z. Ren, Introducing laves phase strengthening into an ultrafine-grained equiatomic CrFeNi alloy by niobium addition, Mater. Sci. Eng. A Struct. Mater. Prop. Microstruct. Process. 806 (2021).
[48] A.W. Zhu, E.A. Starke, Strengthening effect of unshearable particles of finite size: a computer experimental study, Acta Mater. 47 (11) (1999) 3263–3269.
[49] R.V. Goldstein, V.A. Gorodtsov, M.A. Komarova, D.S. Lisovenko, Extreme values of the shear modulus for hexagonal crystals, Scr. Mater. 140 (2017) 55–58.
[50] M.D. Sangid, T. Ezaz, H. Sehitoglu, Energetics of residual dislocations associated with slip-twin and slip-GBs interactions, Mater. Sci. Eng. A Struct. Mater. Prop. Microstruct. Process. 542 (2012) 21–30.
[51] J.E. Bailey, P.B. Hirsch, The dislocation distribution, flow stress, and stored energy in cold-worked polycrystalline silver, Philos. Mag. 5 (53) (1960) 485–497.
[52] E. Khafizova, E. Fakhretdinova, R. Islamgaliev, M. Polenok, V. Sitdikov, H. Yilmazer, Effect of plastic deformation on the structure and mechanical properties of the Zn-4Ag-1Cu zinc alloy, Materials 16 (13) (2023).
[53] P. Wen, L. Jauer, M. Voshage, Y.Z. Chen, R. Poprawe, J.H. Schleifenbaum, Densification behavior of pure Zn metal parts produced by selective laser melting for manufacturing biodegradable implants, J. Mater. Process. Technol. 258 (2018) 128–137.
[54] C. Wang, Y. Hu, C. Zhong, C. Lan, W. Li, X. Wang, Microstructural evolution and mechanical properties of pure Zn fabricated by selective laser melting, Mater. Sci. Eng. A Struct. Mater. Prop. Microstruct. Process. 846 (2022) 143276.
[55] P.K. Bowen, J. Drelich, J. Goldman, Zinc exhibits ideal physiological corrosion behavior for bioabsorbable stents, Adv. Mater. 25 (18) (2013) 2577–2582.
[56] Y. Li, J. Zhou, P. Pavanram, M.A. Leeflang, L.I. Fockaert, B. Pouran, N. Tümer, K. U. Schröder, J.M.C. Mol, H. Weinans, H. Jahr, A.A. Zadpoor, Additively manufactured biodegradable porous magnesium, Acta Biomater. 67 (2018) 378–392.
[57] Y. Li, H. Jahr, X.Y. Zhang, M.A. Leeflang, W. Li, B. Pouran, F.D. Tichelaar, H. Weinans, J. Zhou, A.A. Zadpoor, Biodegradation-affected fatigue behavior of additively manufactured porous magnesium, Addit. Manuf. 28 (2019) 299–311.
[58] Y.W. Yang, C.R. Ling, Y.G. Li, S.P. Peng, D.Q. Xie, L.D. Shen, Z.J. Tian, C.J. Shuai, Microstructure development and biodegradation behavior of additively manufactured Mg-Zn-Gd alloy with LPSO structure, J. Mater. Sci. Technol. 144 (2023) 1–14.
[59] Y. Chen, Z. Xu, C. Smith, J. Sankar, Recent advances on the development of magnesium alloys for biodegradable implants, Acta Biomater. 10 (11) (2014) 4561–4573.
[60] C. Shuai, S. Li, S. Peng, P. Feng, Y. Lai, C. Gao, Biodegradable metallic bone implants, Mater. Chem. Front. 3 (4) (2019) 544–562.
[61] J. Sun, X. Zhang, Z.Z. Shi, X.X. Gao, H.Y. Li, F.Y. Zhao, J.Q. Wang, L.N. Wang, Development of a high-strength Zn-Mn-Mg alloy for ligament reconstruction fixation, Acta Biomater. 119 (2021) 485–498.
[62] Y. Qin, P. Wen, H. Guo, D. Xia, Y. Zheng, L. Jauer, R. Poprawe, M. Voshage, J. H. Schleifenbaum, Additive manufacturing of biodegradable metals: current research status and future perspectives, Acta Biomater. 98 (2019) 3–22.
[63] C.O. Hoog, N. Birbilis, Y. Estrin, Corrosion of pure Mg as a function of grain size and processing route, Adv. Eng. Mater. 10 (6) (2008) 579–582.
[64] G. Ben Hamu, D. Eliezer, L. Wagner, The relation between severe plastic deformation microstructure and corrosion behavior of AZ31 magnesium alloy, J. Alloy. Compd. 468 (1-2) (2009) 222–229.
[65] S. Gollapudi, Grain size distribution effects on the corrosion behaviour of materials, Corros. Sci. 62 (2012) 90–94.
[66] F. Yang, Y. Li, L. Wang, H. Che, X. Zhang, H. Jahr, L. Wang, D. Jiang, H. Huang, J. Wang, Full-thickness osteochondral defect repair using a biodegradable bilayered scaffold of porous zinc and chondr type="periodical"oitin sulfate hydrogel, Bioact. Mater. 32 (2024) 400–414.
[67] D.A. Harrington, P. van den Driessche, Mechanism and equivalent circuits in electrochemical impedance spectroscopy, Electrochim. Acta 56(23) (2011) 8005–8013.
[68] D. Zhao, K. Yu, T. Sun, X. Jing, Y. Wan, K. Chen, H. Gao, Y. Wang, L. Chen, X. Guo, Q. Wei, Material–structure–function integrated additive manufacturing of degradable metallic bone implants for load-bearing applications, Adv. Funct. Mater. 33 (16) (2023) 2213128.
[69] S. Kovacevic, W. Ali, E. Martínez-Pañeda, J. Llorca, Phase-field modeling of pitting and mechanically-assisted corrosion of Mg alloys for biomedical applications, Acta Biomater. 164 (2023) 641–658.
[70] V. Bryzgalov, A.A. Kistanov, E. Khafizova, M. Polenok, A. Izosimov, E. A. Korznikova, Experimental study of corrosion rate supplied with an ab-initio elucidation of corrosion mechanism of biodegradable implants based on Ag-doped Zn alloys, Appl. Surf. Sci. 652 (2024) 159300.
[71] H. Yang, C. Wang, C. Liu, H. Chen, Y. Wu, J. Han, Z. Jia, W. Lin, D. Zhang, W. Li, W. Yuan, H. Guo, H. Li, G. Yang, D. Kong, D. Zhu, K. Takashima, L. Ruan, J. Nie, X. Li, Y. Zheng, Evolution of the degradation mechanism of pure zinc stent in the one-year study of rabbit abdominal aorta model, Biomaterials 145 (2017) 92–105.
[72] M. Mouanga, P. Berçot, J.Y. Rauch, Comparison of corrosion behaviour of zinc in NaCl and in NaOH solutions. Part I: corrosion layer characterization, Corros. Sci. 52 (12) (2010) 3984–3992.

[73] Z. Zhang, A. Liu, J. Fan, M. Wang, J. Dai, X. Jin, H. Deng, X. Wang, Y. Liang, H. Li, Y. Zhao, P. Wen, Y. Li, A drug-loaded composite coating to improve osteogenic and antibacterial properties of Zn-1Mg porous scaffolds as biodegradable bone implants, Bioact. Mater. 27 (2023) 488–504.
[74] D. Xia, Y. Qin, H. Guo, P. Wen, H. Lin, M. Voshage, J.H. Schleifenbaum, Y. Cheng, Y. Zheng, Additively manufactured pure zinc porous scaffolds for critical-sized bone defects of rabbit femur, Bioact. Mater. 19 (2023) 12–23.
[75] J.W. Lee, H.S. Han, K.J. Han, J. Park, H. Jeon, M.R. Ok, H.K. Seok, J.P. Ahn, K. E. Lee, D.H. Lee, S.J. Yang, S.Y. Cho, P.R. Cha, H. Kwon, T.H. Nam, J.H. Lo Han, H. J. Rho, K.S. Lee, Y.C. Kim, D. Mantovani, Long-term clinical study and multiscale analysis of *in vivo* biodegradation mechanism of Mg alloy, Proc. Natl. Acad. Sci. U. S. A. 113 (3) (2016) 716–721.
[76] Z. Zhen, X. Liu, T. Huang, T. Xi, Y. Zheng, Hemolysis and cytotoxicity mechanisms of biodegradable magnesium and its alloys, Biomater. Adv. 46 (2015) 202–206.
[77] B.R. Barrioni, A.C. Oliveira, M. de Fátima Leite, M. de Magalhães Pereira, Sol–gel-derived manganese-releasing bioactive glass as a therapeutic approach for bone tissue engineering, J. Mater. Sci. 52 (15) (2017) 8904–8927.
[78] J. Ma, N. Zhao, D. Zhu, Endothelial cellular responses to biodegradable metal zinc, ACS Biomater. Sci. Eng. 1 (11) (2015) 1174–1182.
[79] J. Wang, F. Witte, T. Xi, Y. Zheng, K. Yang, Y. Yang, D. Zhao, J. Meng, Y. Li, W. Li, K. Chan, L. Qin, Recommendation for modifying current cytotoxicity testing standards for biodegradable magnesium-based materials, Acta Biomater. 21 (2015) 237–249.
[80] I.S. Kwun, Y.E. Cho, R.A. Lomeda, H.I. Shin, J.Y. Choi, Y.H. Kang, J.H. Beattie, Zinc deficiency suppresses matrix mineralization and retards osteogenesis transiently with catch-up possibly through Runx 2 modulation, Bone 46 (3) (2010) 732–741.
[81] W.H. Wang, K.W.K. Yeung, Bone grafts and biomaterials substitutes for bone defect repair: a review, Bioact. Mater. 2 (4) (2017) 224–247.
[82] M. Yamaguchi, Role of zinc in bone metabolism and preventive effect on bone disorder, Biomed. Res. Trace Elem. 18 (4) (2007) 346–366.
[83] X. Gao, Y. Xue, Z. Zhu, J. Chen, Y. Liu, X. Cheng, X. Zhang, J. Wang, X. Pei, Q. Wan, Nanoscale zeolitic imidazolate framework-8 activator of canonical MAPK signaling for bone repair, ACS Appl. Mater. Interfaces 13 (1) (2021) 97–111.
[84] S. Galli, M. Stocchero, M. Andersson, J. Karlsson, W. He, T. Lilin, A. Wennerberg, R. Jimbo, The effect of magnesium on early osseointegration in osteoporotic bone: a histological and gene expression investigation, Breast Cancer Res. Treat. 28 (7) (2017) 2195–2205.
[85] Y. Dou, N. Li, Y. Zheng, Z. Ge, Effects of fluctuant magnesium concentration on phenotype of the primary chondrocytes, J. Biomed. Mater. Res. Part A 102 (12) (2014) 4455–4463.
[86] L. Zhang, C. Yang, J. Li, Y. Zhu, X. Zhang, High extracellular magnesium inhibits mineralized matrix deposition and modulates intracellular calcium signaling in human bone marrow-derived mesenchymal stem cells, Biochem. Biophys. Res. Commun. 450 (4) (2014) 1390–1395.
[87] H. Jin, S. Zhao, R. Guillory, P.K. Bowen, Z. Yin, A. Griebel, J. Schaffer, E.J. Earley, J. Goldman, J.W. Drelich, Novel high-strength, low-alloys Zn-Mg (<0.1wt% Mg) and their arterial biodegradation, Mater. Sci. Eng. C 84 (2018) 67–79.
[88] C. Chen, H. Huang, J. Niu, J.F. Nie, G. Yuan, Origin of high tension-compression yield asymmetry in as-extruded pure zinc, Scr. Mater. 200 (2021).
[89] M. Hussain, S. Ullah, M.R. Raza, N. Abbas, A. Ali, Recent developments in Zn-based biodegradable materials for biomedical applications, J. Funct. Biomater. 14 (1) (2023) 1–21.